The Astrophysical Journal, 711:75–98, 2010 March 1 doi:10.1088/0004-637X/711/1/75

PHYSICAL CONDITIONS IN A CORONAL MASS EJECTION FROM *HINODE*, *STEREO*, AND *SOHO* OBSERVATIONS

E. Landi[1], J. C. Raymond[2], M. P. Miralles[2], and H. Hara[3]
[1] Naval Research Laboratory, Washington, DC 20375, USA
[2] Harvard-Smithsonian Center for Astrophysics, 60 Garden St., Cambridge, MA 02138, USA
[3] National Astronomical Observatory of Japan, Osawa, Mitaka, Tokyo 181-8588, Japan
Received 2009 July 8; accepted 2010 January 15; published 2010 February 5

ABSTRACT

In the present work, we analyze multiwavelength observations from *Hinode*, *Solar and Heliospheric Observatory* (*SOHO*), and *STEREO* of the early phases of a coronal mass ejection (CME). We use *Hinode*/EIS and *SOHO*/UVCS high-resolution spectra to measure the physical properties of the CME ejecta as a function of time at 1.1 and 1.9 solar radii. *Hinode*/XRT images are used in combination with EIS spectra to constrain the high temperature plasma properties of the ejecta. SECCHI/EUVI, SECCHI/COR 1, *SOHO*/EIT, and *SOHO*/LASCO images are used to measure the CME trajectory, velocity, and acceleration. The combination of measurements of plane of the sky velocities from two different directions allows us to determine the total velocity of the CME plasma up to 5 solar radii. Plasma properties, dynamical status, thermal structure, and brightness distributions are used to constrain the energy content of the CME plasma and to determine the heating rate. We find that the heating is larger than the kinetic energy, and compare it to theoretical predictions from models of CME plasma heating and acceleration.

Key words: Sun: activity – Sun: corona – Sun: coronal mass ejections (CMEs) – Sun: UV radiation – techniques: spectroscopic

1. INTRODUCTION

Coronal mass ejections (CMEs) are the most spectacular and energetic events in the solar system. They are triggered by the sudden acceleration of large amounts of plasma in the solar atmosphere that are released in the heliosphere. The ejected mass is in the 10^{14}–10^{16} g range, and velocities can exceed 2000 km s^{-1}. CMEs typically are made of three components: an outer shell of fast plasma, a cavity within the shell, and a core where often an erupting prominence is located. A large body of observations and theoretical work has been devoted to CMEs, and several advances toward understanding them have been made. However, how the corona is able to generate, accelerate, and heat CME plasmas largely remains a mystery.

Theoretical models that attempt to explain CME acceleration can be divided into two main classes. One class requires the sudden release of external energy as a trigger to the acceleration of plasma previously in equilibrium; the second class involves the slow storage of magnetic energy in the pre-CME plasma as the pre-requisite for a sudden release and the CME acceleration. Reviews of these models can be found in Klimchuk (2001), Zhang & Low (2005), and Forbes et al. (2006).

Relatively little is known about the heating of CME plasma after it is ejected from the Sun. A few studies based on UVCS spectra show that the integrated post-eruption heating is comparable to the kinetic energy of the plasma, so that heating plays a major role in the energy budget (Akmal et al. 2001; Ciaravella et al. 2001; Bemporad et al. 2007; Lee et al. 2009). A similar result was found from the ionization state of gas measured at 1 AU with the *Advanced Composition Explorer* (*ACE*; Rakowski et al. 2007). Filippov & Koutchmy (2002) also found that substantial heating is needed to explain how the erupting filament changes from absorption to emission in EIT images. Possible heating mechanisms include wave heating, thermal conduction, shock waves, or dissipation of magnetic energy as the flux rope relaxes to a lower free energy state. The relative importance and the viability of such mechanisms need to be determined from observations.

One of the main problems in CME science has been the lack of observations of the very early stages of the CME development. With few exceptions, acceleration takes place within around two solar radii above the solar surface, but CMEs are identified in space by coronographs, at larger distances from the solar disk as determined by the occulting disk. Such observations miss the most crucial phase of CME initiation. Narrowband imagers that take high cadence observations of the solar disk can help identifying CME initiation, but their diagnostic capabilities are limited. Stigmatic spectrometers complement narrowband imagers, because of their diagnostic potential and simultaneous multi-temperature coverage of the observed plasma. The application of spectroscopic diagnostics to measure plasma parameters such as density, temperature, composition, and bulk speed at many temperatures simultaneously in the 10^4–10^7 K range during the initial phases can provide vital insight into CME plasma heating and acceleration. However, such measurements have been rather scarce in the past, because of the difficulty of detecting the CME initial phases within the narrow field of view of the slit of a high-resolution spectrometer.

The aim of the present work is to measure the physical properties of a CME during the initial phases of acceleration. We used "sit'n'stare" observations of *Hinode*/EIS at $\simeq$1.1 $R_\odot$, and *SOHO*/UVCS at $\simeq$1.9 $R_\odot$, and combined them with simultaneous time sequences from *Hinode*/XRT, *STEREO-A*/EUVI, and *SOHO*/EIT to obtain detailed information on dynamic evolution, trajectory, thermal structure, electron density, and heating of the CME ejecta as they were leaving the Sun. The difference in the line-of-sight direction between *Hinode* and *SOHO* from L1/Earth, and *STEREO-A* 24.°3 to the west allowed us to reconstruct the three-dimensional trajectory and velocity of the CME. Additional information was derived from *SOHO*/LASCO and

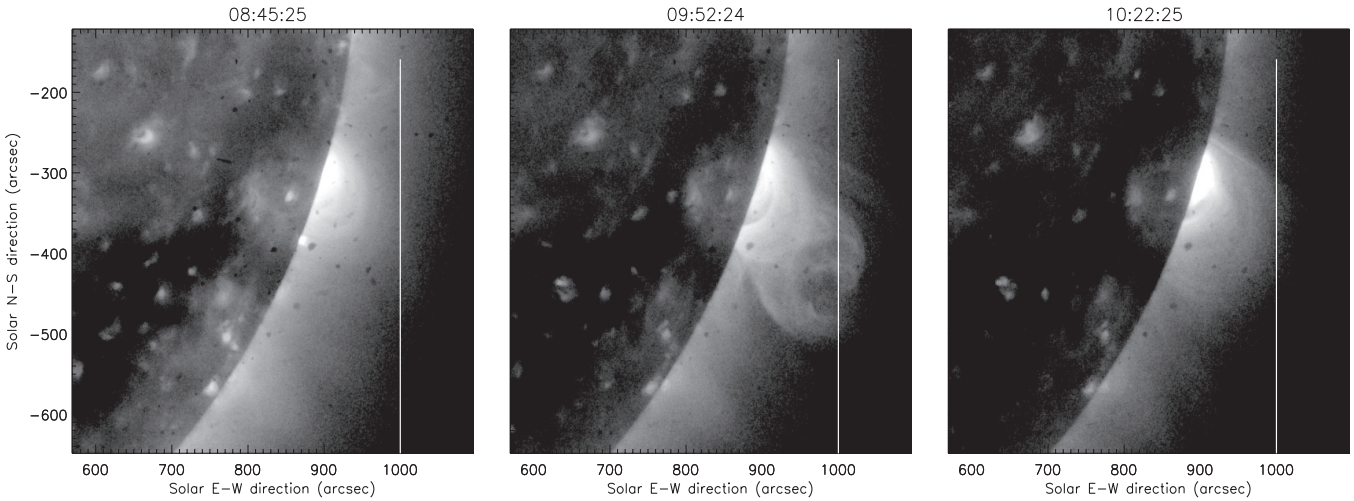

Figure 1. *Hinode*/XRT images of the SW quadrant of the Sun, with the EIS slit superimposed. XRT images were taken before, during and after the CME event. The southern edge of the EIS slit stretches beyond the XRT field of view, down to $Y = -670''$.

Table 1
Summary of Observations

Satellite	Separation Angle	Instrument	Height (R_{sun})	Core	Front	Observation Type
SOHO	0	EIT	1.0–1.5	Y		λ195 images
		UVCS	1.9	Y		H I Ly-α profile
		LASCO	1.5–30	Y		White light images
Hinode	0	EIS	1.1	Y		λ170–212, λ245–292 spectra
		XRT	1.0–1.3	Y		X-ray images
STEREO-A	24.3	EUVI-A	1.0–1.7	Y	Y	λ304, λ171, λ195, λ284 images
		COR 1A	1.4–4.0	Y	Y	White light images
		COR 2A	2.5–15	Y		White light images

Note. The separation angle is taken from the Sun–Earth direction, and it is positive westward.

STEREO-A/COR 1. The CME that we studied was observed on 2008 April 9 during the *Whole Heliospheric Interval* coordinated campaign.

The present measurements are intended to provide theoreticians with experimental benchmarks on the dynamics and the heating of CME plasma at the very beginning of a CME event. The observations are described in Section 2, and the plasma parameters and evolution of the rising CME ejecta are described in Section 3. Measurements are used to determine the energy budget and compare it to theoretical predictions in Section 4. Results are summarized in Section 5.

2. OBSERVATIONS

The CME we observed was activated at around 9:10 UT on 2008 April 9, and consisted of the standard three components: a fast front, a cavity, and a core which hosted an erupting prominence. Different instruments observed different portions of the CME, as shown in Table 1. The cavity was visible with the EUV imagers, but it was too faint to carry out any plasma diagnostics. The position of the CME was behind the solar limb as seen by *STEREO-B*, so that only *STEREO-A* data could be used.

2.1. EIS Observations

EIS carried out sit'n'stare observations that included the entire wavelength range, with a 10 minute cadence (600 s exposure time). Observations were made on 2008 April 9, between 06:20 UT and 13:55 UT, with a field of view of $2'' \times 512''$. The slit was centered at $(1000'',-412'')$ and stretched in the north–south direction; its field of view included an active region in its top half. The EIS field of view is shown in Figure 1, superimposed to a sequence of three *Hinode*/XRT images. A description of the EIS instrument can be found in Culhane et al. (2007). EIS observations were carried out continuously, but problems in the telemetry rate caused the data to be initially lost and recovered later in a non-standard format. The recovered data consisted of 1024×512 pixel quadrants, and they were recovered for almost all data sets in the 06:20 UT to 13:55 UT time interval. From time to time, however, a few data gaps made a few quadrants unavailable. After 13:35 UT, the available data quadrants decrease until none were available after 13:55 UT.

The data were not in a standard FITS format, and the EIS preparation routines available in *SolarSoft* could not be applied. We have done the basic data reduction applying individual routines to the raw data. We first de-biased the data, using the same algorithm as the standard program EIS_PREP.PRO. Then we developed an algorithm to remove both cosmic rays and warm and hot pixels. This procedure first recognizes the presence of a warm or hot pixel by comparing the intensity of each pixel to the median of the intensity of the nearest neighbor pixels. Pixels with values larger than 4 times the median value were flagged to build an empirical map of the warm and hot pixels. This procedure also flagged most cosmic rays: the long exposure time of each EIS data set ensured that a large number of them were present in the field of view. The intensity of the

Table 2
Details of the Observations Carried Out by *STEREO-A*/EUVI, *Hinode*/XRT, and *SOHO*/EIT

Quantity	EUVI-A				XRT	EIT
FOV center	(0″, 0″)	(0″, 0″)	(0″, 0″)	(0″, 0″)	(833″, −384″)	(0″, 0″)
Filter	304 Å	171 Å	195 Å	284 Å	Al-poly	195 Å
FOV size	Full Sun	Full Sun	Full Sun	Full Sun	512″ × 512″	Full Sun
Cadence	10 m	2.5 m	10 m	20 m	1 m	12 m
Pixel size	1.″59	1.″59	1.″59	1.″59	1.″03	5.″26

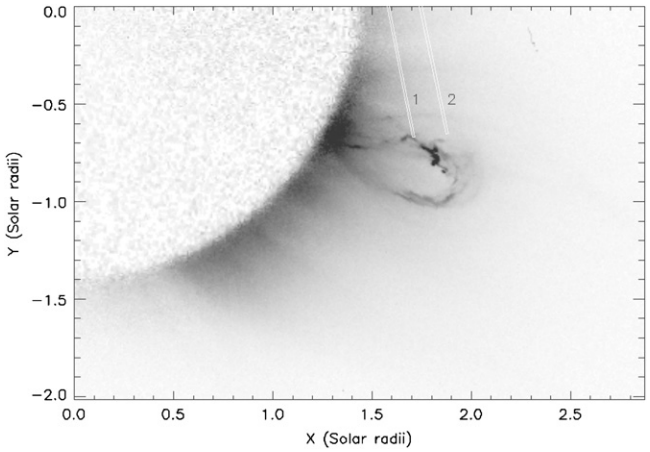

Figure 2. COR 1A image of the CME observed at 10:45 UT on 2008 April 9. The positions 1 and 2 of the UVCS slit mark two different locations along the UVCS line of sight corresponding to the SOHO plane of the sky (1) and 0.4 $R_{\rm sun}$ behind it (2), projected in *STEREO-A*'s plane of the sky. The CME ejecta intercept the UVCS line of sight between these two points. Coordinates are from the Sun's center.

flagged pixels was replaced with the median of the intensity of the nearest neighbors. A similar procedure was then applied to the residual cosmic rays by considering the values of each pixel along the EIS time series of observations. Pixels whose intensity was more than 4 times the median of all EIS observations were replaced with the median of the intensity of the nearest neighbor pixels in the same frame. The threshold detection value of 4 used for both cosmic rays and warm and hot pixels was selected by trial and error, in a compromise between the effort of eliminating all "bad" pixels, and the need of sparing bright pixels due to real solar features.

The reduced data consisted of a series of full images of the entire EIS spectrum in counts s^{-1}, although some 1024 pixel wide quadrants were still missing. Line intensities were determined summing all counts under the line profiles, and subtracting the background. For strong and isolated lines used to measure Doppler shifts, we have fitted a Gaussian line profile to determine line centroid and width. Intensities were converted into photon cm^{-2} s^{-1} $arcsec^{-2}$ using the intensity calibration of Brown et al. (2008).

2.2. UVCS Observations

UVCS observations were made continuously during 2008 April 9. The slit was positioned at a heliocentric height of 1.7 $R_\odot$ at the west limb (P.A. = 279° in radial direction normal to the slit). The data reported here were taken with the O VI channel. The instrument configuration for the observations included an entrance slit of 50 μm, a spatial binning of 4 pixels (28″) for H I Ly$\alpha\lambda$1215.67, a spectral binning of 1 pixel (0.0915 Å), and an instantaneous field of view of 40′ × 14″. A long series of 120 s exposures was obtained, with a 10 s readout after each exposure. For a description of the UVCS instrument, see Kohl et al. (1995, 2006). Details concerning the analysis of UVCS data are given by Gardner et al. (1996, 2000, 2002) and Kohl et al. (1997, 1999). The UVCS Data Analysis Software (DAS) was used to remove image distortion and to calibrate the data in wavelength and intensity. Figure 2 shows a COR 1A image of the CME observed at 10:45 UT on 2008 April 9. The positions 1 and 2 of the UVCS slit mark two different locations along the UVCS line of sight corresponding to the *SOHO* plane of the sky (1) and 0.4 $R_{\rm sun}$ behind it (2), projected in *STEREO-A*'s plane of the sky. The CME ejecta intercept the UVCS line of sight between these two points.

2.3. EIT, EUVI-A, and XRT Observations

SOHO/EIT, SECCHI/EUVI-A, and *Hinode*/XRT were carrying out observing sequences that allowed us to monitor the initial phases of the CME ejecta. During the event, EUVI-A was carrying out observations of the full Sun at full resolution, with all filters. XRT was observing the southwest (SW) quadrant of the Sun, centered at $X = 833''$, $Y = -384''$, with a 1 minute cadence, with only one filter, Al-poly. EIT observed the full solar disk with approximately 12 minute cadence, using the λ195 filter and a reduced spatial resolution of 5.″26. Details for all these instruments also listed in Table 2. EIT, XRT, and EUVI-A data were reduced using the standard software available for each instrument in *SolarSoft*. The angle between the lines of sight of XRT and EIT on one side and EUVI-A on the other was 24.°3.

2.4. LASCO, COR 1A, and COR 2A Observations

SOHO/LASCO, SECCHI/COR 1A, and COR 2A were carrying out observations that could be used to monitor the evolution in space of the CME ejecta once they left the field of view of EIS, XRT, and EUVI-A. LASCO C2 and C3 images were used to determine the velocity and acceleration of the CME front as a function of time from 3 to 22 solar radii. The C2 images taken close to the time of the CME event have a cadence of 20–30 minutes.

SECCHI/COR 1A images obtained with a 10 minute cadence were used to determine both the velocity of the CME and the column density of the emitting material from 1.4 to 6 solar radii. SECCHI/COR 2A extended this field of view to 15 $R_{\rm sun}$, with a cadence of $\simeq$30 minutes. All images were reduced using the standard software available in *SolarSoft*.

3. PLASMA DIAGNOSTICS

Plasma diagnostics with high-resolution spectra from EIS and UVCS could only be carried out on the bright core, as the other two components left no signatures in the spectra. The CME front could be observed with EUVI-A and COR 1A, before it became too faint, and we could measure its trajectory and velocity in the *STEREO-A* plane of the sky. The core could be observed with all instruments. Since *STEREO-A* observed the Sun from a

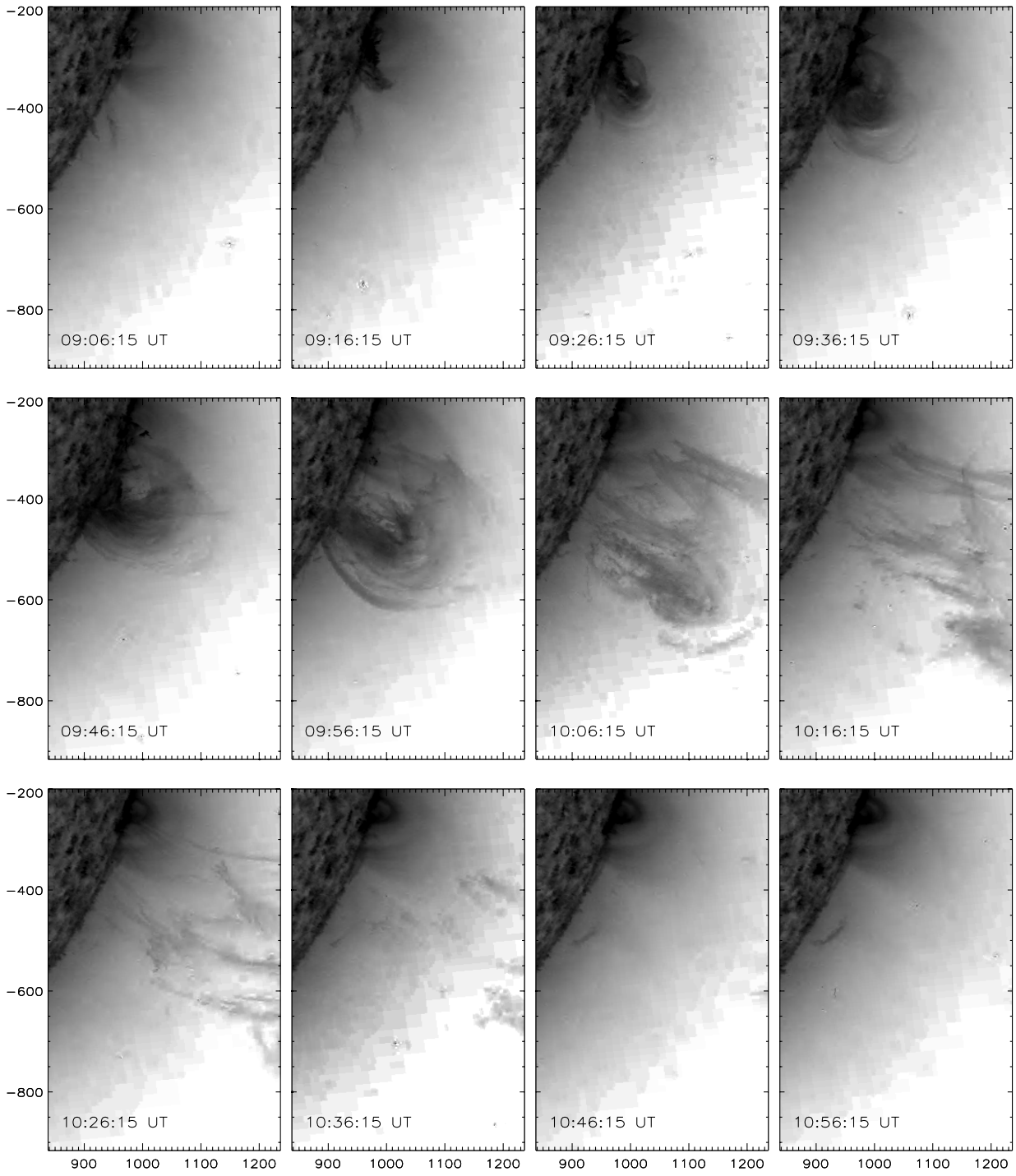

Figure 3. Time series of *STEREO-A* EUVI-A 304 Å images of the CME event. Coordinates are in arcseconds, from the Sun's center.

different direction than *SOHO* and *Hinode*, we could reconstruct the three-dimensional trajectory and velocity of the CME core up to 6 $R_{\rm sun}$. LASCO data allowed us to extend the velocity measurements of the core in the *SOHO* plane of the sky up to 22 solar radii. Doppler shifts from UVCS and EIS provided an independent determination of the total velocity at 1.1 and 1.9 solar radii.

By looking at X-rays, XRT observed a different kind of emission that seems to be loosely associated with the core (see the following section). XRT data will be used to discuss the presence of plasma at very high temperature and its relation to the core of the CME.

The analysis of spectral line intensities requires the use of large amounts of atomic data; in the present work, we have used Version 6 of the CHIANTI database (Dere et al. 1997, 2009). The ion abundances of Bryans et al. (2009) and the coronal abundances of Feldman et al. (1992) have been used to calculate line emissivities.

3.1. CME Morphology

3.1.1. XRT, EIT, and EUVI-A Images

Figures 3–6 show time series of the SW quadrant of the solar atmosphere with the λ304, λ171, and λ284 EUVI-A filters and

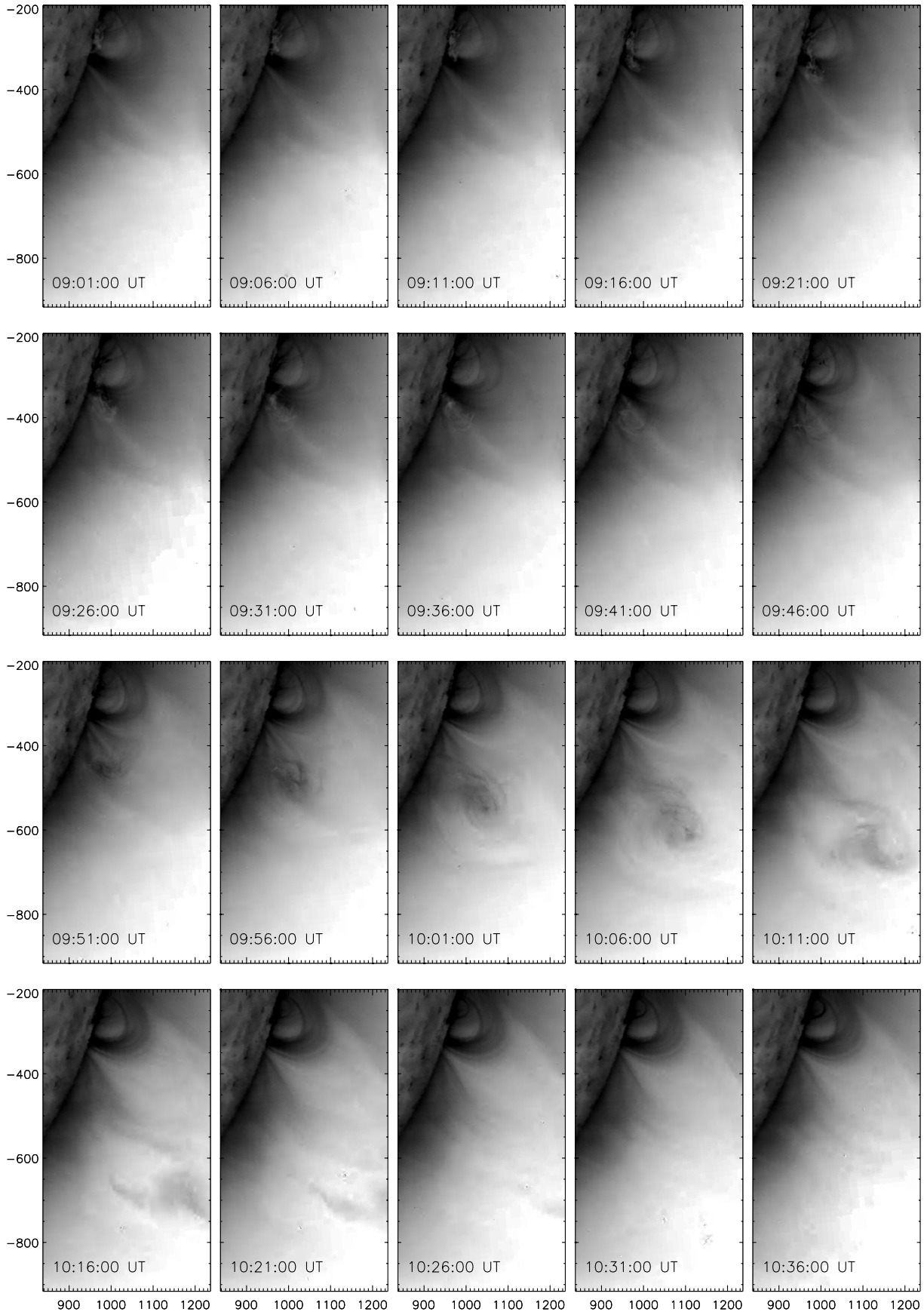

Figure 4. Time series of *STEREO-A* EUVI-A 171 Å images of the CME event. Coordinates are in arcseconds, from the Sun's center.

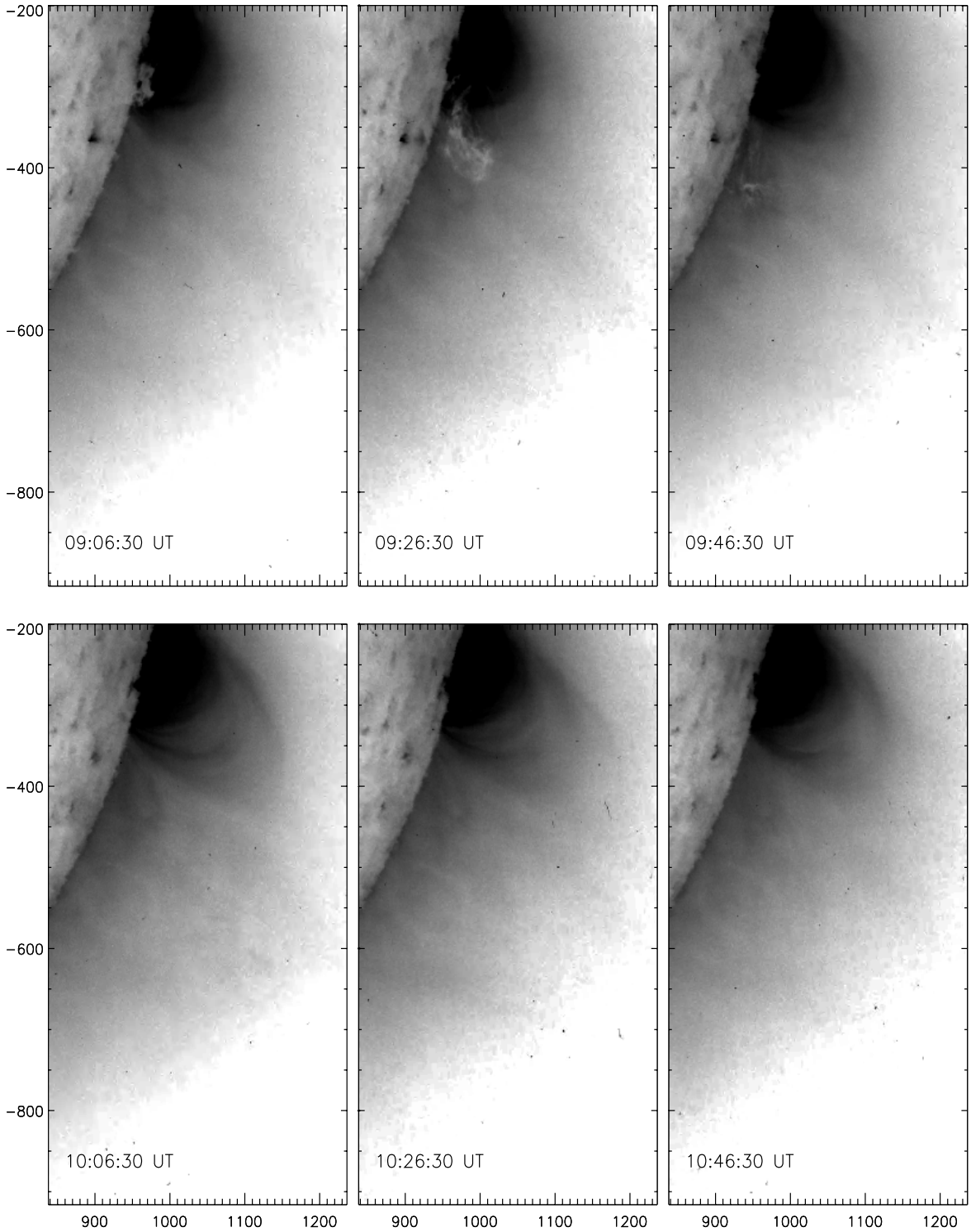

Figure 5. Time series of *STEREO-A* EUVI-A 284 Å images of the CME event. Coordinates are in arcseconds, from the Sun's center.

with the XRT Al-poly channel. The EUVI-A λ195 and EIT λ195 channels showed qualitatively similar results to the λ171 channel in EUVI-A. We only showed a few of the available images to save space, without losing the relevant information. Both instruments, until ≃9:10 UT, show a rather quiescent active region at the west limb. EUVI-A, thanks to its viewing angle, could see the active region face-on showing the presence of a filament in emission with the 304 Å channel and in absorption with the other three channels. XRT and EIT (not shown here) could instead only see the top of the active region, which had already crossed the limb from their viewing angle. At around 9:10 UT this filament activated and initially, after briefly rising in altitude, it moved south. At around 9:30 UT, this filament changed direction and started a rapidly accelerating upward movement, giving rise to the eruption. The ejected material was also seen with XRT and EIT and traveled out the field of view of the three instruments after ≃10:30 UT. Although the active region hosting the filament experienced changes as a result of

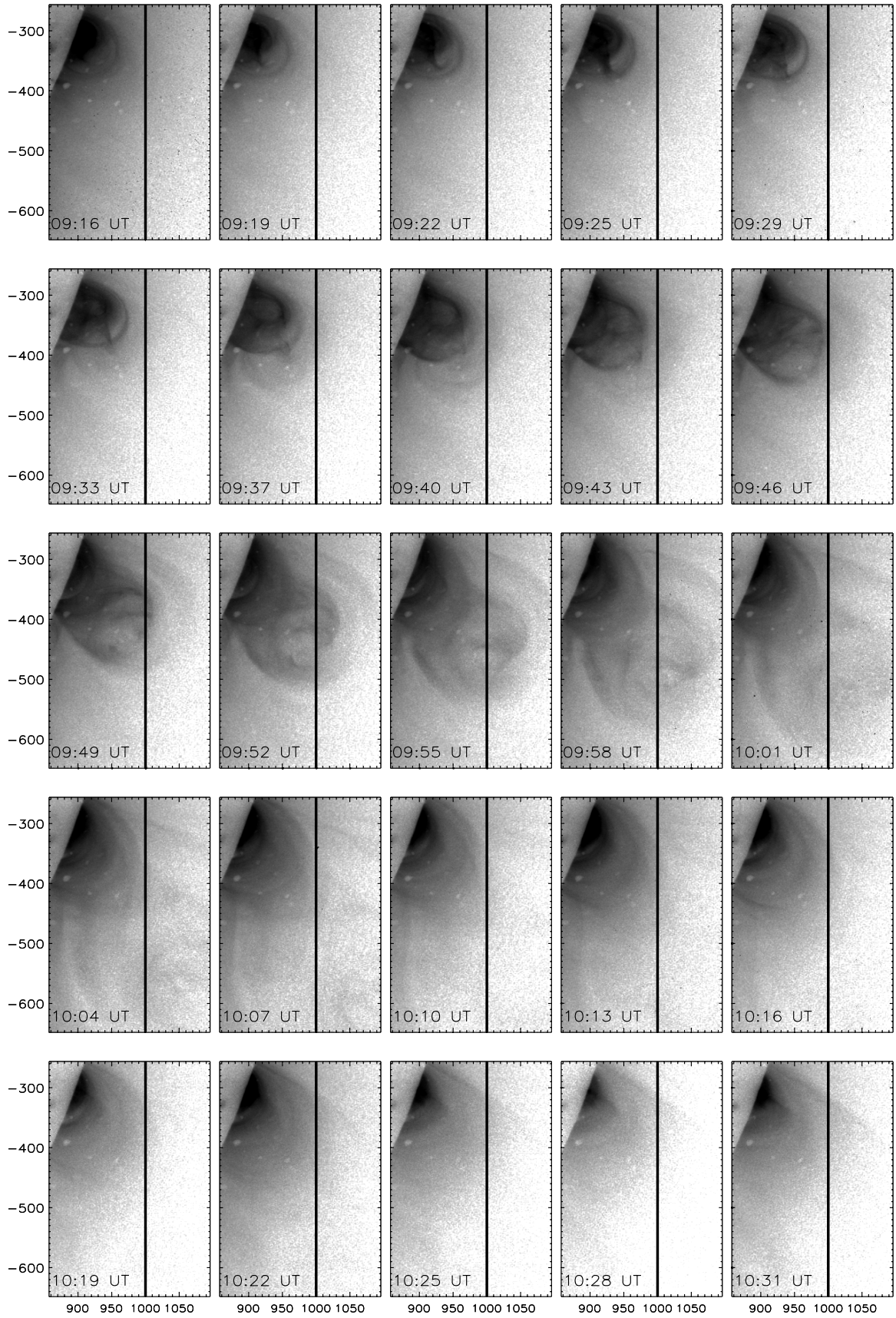

Figure 6. Time series of *Hinode*/XRT Al-poly images of the CME event. The EIS slit field of view is superimposed to the XRT image (vertical solid line). Coordinates are in arcseconds, from the Sun's center.

the CME ejection, no major flare was detected during the CME event, perhaps because the event took place behind the limb from the viewpoints of the X-ray telescopes.

At the same time when the filament started its outward trajectory, it also changed its appearance in the EUVI-A images. In fact, until that time the filament was seen in absorption, but after 9:30 UT the absorption feature fades away and the filament became brighter, and it was seen as an *emission* feature. The strength of the emission was different in the EUVI-A channels. In the λ304 channel, the CME core was visible in emission at all times, was much larger in size than was seen earlier in absorption, expanded as it traveled away from the limb, and had a very filamentary structure. In the λ171 channel, the filament was visible as an approximately circular structure of $\simeq 100''$ in diameter, rotating around an axis perpendicular to the plane of the sky, and surrounded by fainter material. The EUVI-A and EIT emission in the λ195 channel was much fainter but similar in shape to that at 171 Å. In the λ284 channel, the filament was visible in absorption, but it became barely visible in emission at the same time, and with the same shape, when it appeared in emission in the other channels. Activity also became visible in XRT images after 9:40 UT, when the CME core started to take off. XRT also observed the core in emission and not in absorption, even though their shape was different than those seen by EUVI-A. Since the active region was placed behind the limb as seen by *SOHO* and *Hinode*, XRT, and EIT could not see the initial phases of prominence activation.

The change from absorption to emission for the CME plasma is very important, as it indicates that free-bound absorption, due to neutral H and He, or He II, was no longer active. This means that by the time the CME core took off, it was also being heated to temperatures where H and He are sufficiently ionized to stop absorbing radiation. The similarity in shape and timing of the emission feature in the EUVI-A λ171, λ195, and λ284 channels suggests that it was the same plasma that produced the additional emission. However, the bandpasses of all three channels include lines formed at very different temperature ranges. In order to understand the thermal structure of the emission feature it is necessary to use diagnostic results from spectrometers.

Even more intriguing is the emission from the CME ejecta observed by XRT. The XRT Al-poly wave band includes soft X-ray emission below 50 Å, which is most sensitive to multimillion degree plasmas, emitted by active region and flares (Golub et al. 2007), and a small component between 179 and 190 Å. The presence of emission in the XRT images of the CME plasma could be due to two different causes: (1) multimillion degree plasma was present in the ejected plasma already at the very beginning of the CME acceleration or (2) the sensitivity of the XRT Al-poly filter to emission from colder material is larger than expected for a filter centered in the soft X-rays. We will discuss both scenarios in Section 3.6.

The relation between the XRT emission and the CME core can be seen in Figure 7, where the EIT λ195 emission is overlaid on the XRT images taken at the same time. Figure 7 shows that the two plasmas were not co-spatial, and that the EIT erupting prominence was (1) ahead of the XRT plasma, and (2) brighter where XRT emission was fainter. The relative position of these two plasmas and its significance will also be discussed in Section 3.6.

3.1.2. EIS Time–Intensity Images

The EIS intensity distribution along the slit helped us to understand the temperature of the CME plasma even before detailed plasma diagnostics are applied to line intensities. Figure 8 shows an intensity versus time image of the emitting plasma built in the following way. Since EIS used the $2''$ wide slit in sit'n'stare mode, it is not possible to build two-dimensional images of the region. However, by placing side by side consecutive images of the $2''$ slit obtained integrating the intensity of a given line, an image where the *Y*-axis is the intensity along the slit and the *X*-axis is the time it can be built, that allows us to monitor the evolution of the CME material as it passes through the EIS field of view. The advantage of these images is that they can be built with any line in the EIS spectrum, regardless of their temperature of formation. In Figure 8, we have built such an image with 12 lines from ions formed at very different temperatures: 5.2×10^4 K (He II), 2.3×10^5 K (O V), 2.8×10^5 K (Mg V), 3.6×10^5 K (Fe VIII), 7.4×10^5 K (Fe IX), 1.1×10^6 K (Fe X), 1.3×10^6 K (Fe XI), 1.5×10^6 K (Fe XII), 1.8×10^6 K (Fe XIII), 2.2×10^6 K (Fe XV), 2.7×10^6 K (Fe XVI), and 4.1×10^6 K (Fe XVII). Such images show that the CME core was much brighter than the background in the ions formed below 1 MK, at transition region temperatures. The CME ejecta first appeared in the spectrum taken between 9:30 UT and 9:40 UT, and were last seen in the spectrum taken between 10:00 UT and 10:10 UT for a total of four consecutive spectra. Intensity images from ions formed at 1–2 MK (typical of quiet Sun and active region temperatures) show that the ejecta either were very faint or they are seen as a decrease of intensity. This decrease, however, was not due to H or He absorption, otherwise it would have been visible in the EUVI-A images as well. Rather, the lower emission was due to the lack of emitting coronal material, which was displaced by the passing CME. Very faint traces of the CME are present in the Fe XV, XVI, XVII lines at the time and location of the CME event as seen in the colder lines, but not in lines emitted at higher temperatures (Ca XV, XVI, Fe XXII-XXIV), indicating that the amount of plasma in the CME ejecta that reached multimillion temperatures, if any, was rather small. This will be discussed in more detail in Section 3.6.

One further indication that the bulk of the CME plasma did not reach very high temperatures is given by continuum emission. The CME plasma could emit detectable free–free continuum radiation if its emission measure is sufficiently large and the temperature exceeds $\simeq 1$ MK. Such emission can be observed in both EIS bands and is expected to have similar intensity levels in both bands. Intensity versus time images of the EIS continuum at six different wavelengths are shown in Figure 9; three of them were taken in the short wavelength band, the other three in the long wavelength band. The CME core was visible *only* in the short wavelength range. This means that the continuum emission is recombination continuum from bare He recombining into He II rather than free–free emission. Since the edge of the He II recombination continuum lies at $\simeq 227.8$ Å, it can only be detected in the EIS short wavelength channel, as observed in Figure 9. This indicates that the bulk of the CME ejecta plasma has been indeed heated from the cold prominence temperatures, but only up to a few hundred of thousand degrees.

Figure 8 also shows that the CME ejecta were observed in emission from lines that are formed, when the plasma is in ionization equilibrium, almost one order of magnitude apart in temperature. Is this due to the plasma being out of equilibrium, or were lines from different ions emitted by separate plasma elements in the ejecta? To investigate this, we have compared the normalized intensity profiles of a few bright lines emitted by the CME ejecta. This comparison is displayed in Figure 10, where the normalized intensities of lines from He II, O V, O VI,

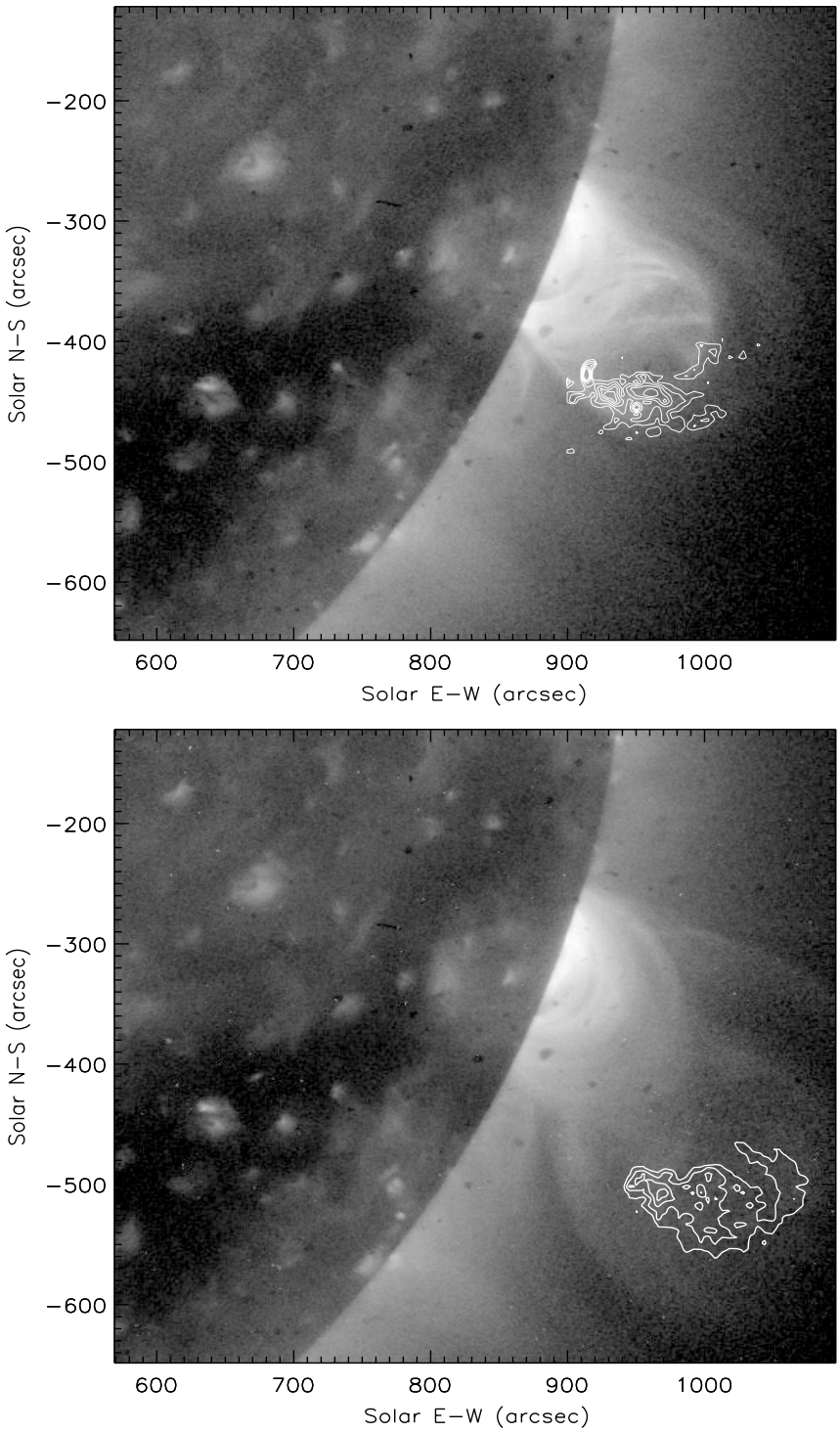

Figure 7. XRT images taken at 9:40 UT (top) and 10:00 UT (bottom), with contours of the EIT λ195 emission from the CME core observed at the same time.

Si VII, and Fe VIII are shown. These line intensities have been cleaned of background emission, determined by fitting a second-order polynomial at locations outside the CME ejecta and then subtracted. The temperature of formation under equilibrium conditions of these ions ranges from ≃50,000 K to almost 600,000 K, and yet their intensity profiles are very similar. This can be consistent with two possible scenarios: line intensities were emitted by a single plasma element whose conditions were far from ionization equilibrium, or they were emitted by different plasmas moving coherently in the same direction. However, the time to approach ionization equilibrium is around $10^{12}/N_e$ seconds, or 10–100 s for the densities derived in Section 3.3. This is less than a tenth the expansion timescale, so the first scenario is less likely.

3.2. Dynamics and Trajectory

Having observations from two different directions allowed us to reconstruct the three-dimensional trajectory of the CME and its total velocity and acceleration. The data allowed us to do this for the core of the CME, from its first appearance in the EIT

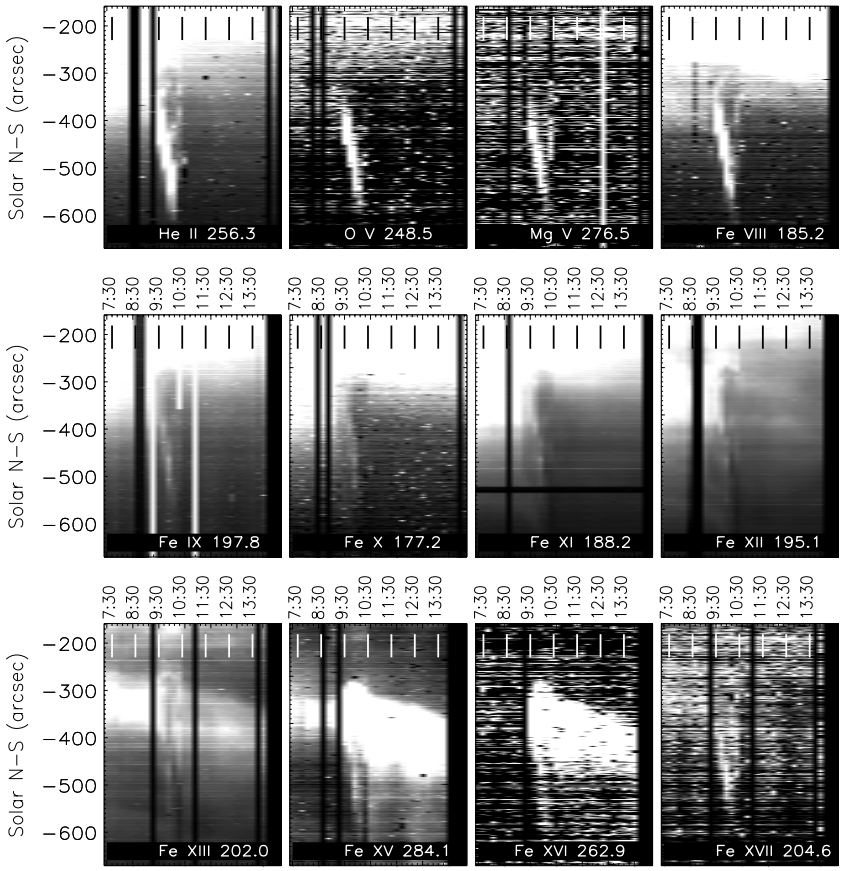

Figure 8. Intensity–time images from 12 lines in the EIS wavelength range. The pixels along the slit direction have been summed in groups of 10 to improve the image. The temperature of the formation of the lines is 5.2×10^4 K (He II), 2.3×10^5 K (O V), 2.8×10^5 K (Mg V), 3.6×10^5 K (Fe VIII), 7.4×10^5 K (Fe IX), 1.1×10^6 K (Fe X), 1.3×10^6 K (Fe XI), 1.5×10^6 K (Fe XII), 1.8×10^6 K (Fe XIII), 2.2×10^6 K (Fe XV), 2.7×10^6 K (Fe XVI), and 4.1×10^6 K (Fe XVII).

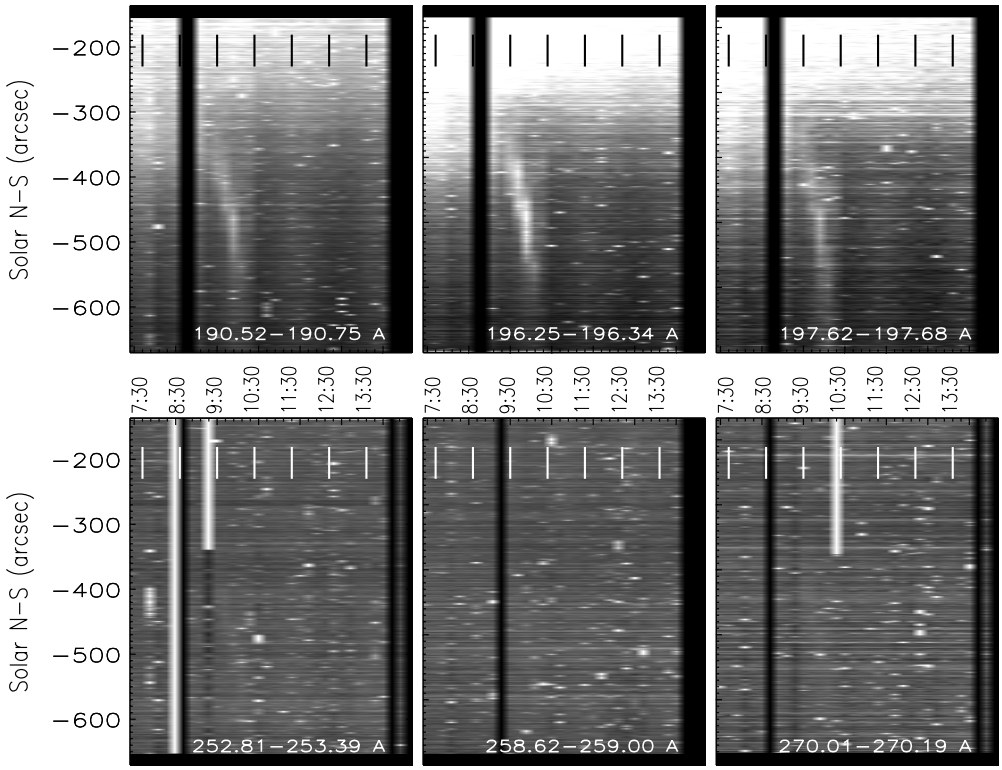

Figure 9. Intensity–time images of EIS continuum emission seen in six different wavelength ranges. The three windows in the top row are in the EIS-SW band, the bottom three are in the EIS-LW band.

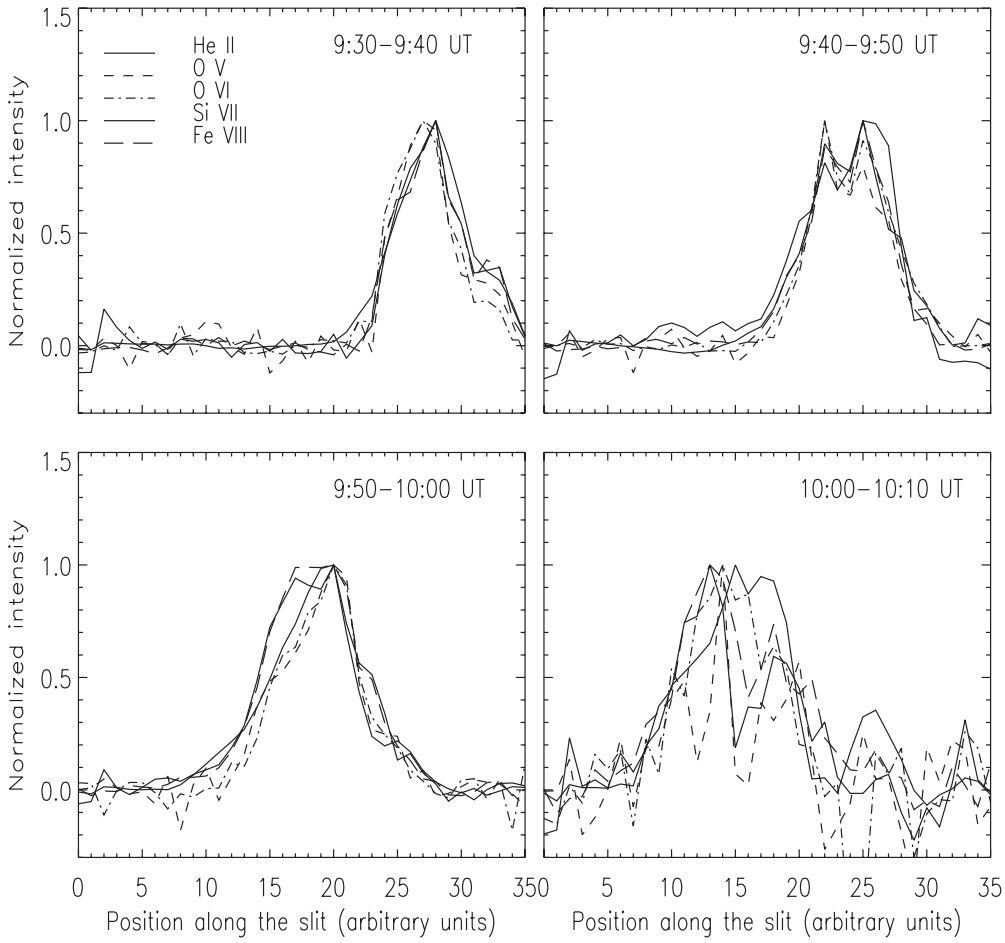

Figure 10. Normalized intensity profiles along the EIS slit of He II, O V, O VI, Si VII, and Fe VIII lines as a function of time.

field of view up to $\simeq 6$ $R_{\rm sun}$. Additional measurements of the core trajectory projected on the *SOHO* plane of the sky from 6 to $\simeq 22$ $R_{\rm sun}$ could be done using LASCO C3 data. The CME front was observed only by EUVI-A and COR 1A, so we could only follow its trajectory projected in the *STEREO-A* plane of the sky.

3.2.1. CME Core Trajectory and Velocity

The three-dimensional trajectory of the core could be reconstructed by combining simultaneous observations of EIT and LASCO on one side, and EUVI-A, COR 1A, and COR 2A on the other, assuming that the plasma imaged by those *Hinode* and *SOHO* instruments is the same. The core faded away in the COR 2A field of view at $\simeq 5$ $R_{\rm sun}$, and this is the limit that our reconstruction can reach. In each pair of images, we measured the position of the outer edge of the core, and by simple geometrical considerations we determined the polar coordinates (R, α, β) of the measured point, where the meaning of these three quantities is shown in Figure 11. The values of (R, α, β) we measured are listed in Table 3.

Figure 12 shows the CME core trajectory both in three-dimensional and projected in the plane of the ecliptic, along with the directions of the *STEREO-A* and *SOHO* planes of the sky: after an initial slight deviation toward the Earth, the CME goes approximately along a straight path, within uncertainties. It is important to note that the CME is slowly moving away from the Earth's direction.

The measurements in Table 3 allow us to measure the total velocity of the CME core, whose absolute value is displayed in Figure 13 (top). The CME core is very abruptly accelerated at very low altitudes, and then its velocity increases more gradually at distances larger than 2 solar radii. It is difficult to associate uncertainties with such velocity estimates, due to the approximations involved in their measurements. Beyond 5 solar radii, we do not have data from *STEREO-A*, so we can only measure the projection of the velocity on the *SOHO* plane of the sky with LASCO. The results are shown in Figure 13 (bottom). The velocity is approximately constant beyond 5 solar radii, although there is a notable scattering. The uncertainties in the measurements prevent us from determining whether individual velocity variations are artifacts of the uncertainties or due to true acceleration. Overall, the CME core travels with a constant velocity of $\simeq$450 km s^{-1} in the *SOHO* plane of the sky. If we assume that the angle φ is constant, the absolute value of the total velocity of the CME core is $\simeq$475 km s^{-1}.

3.2.2. CME Front Velocity

The velocity of the CME front could only be determined using EUVI-A and COR 1A, since neither EIT nor LASCO could unambiguously identify it; moreover, it could only be determined up to 10:45 UT, before it fades away in the COR 1A image at the altitude of $\simeq 3$ $R_{\rm sun}$. Velocity and acceleration are shown in Figure 14. However, since there are considerable uncertainties in the velocity determinations, the values of the

Table 3
Three-dimensional Reconstruction of the Trajectory of the CME Core

Instrument	*SOHO*			Instrument	*STEREO-A*			R	θ	φ
	Time	Y	Z		Time	Y	Z			
EIT	9:24	1.00	−0.41	EUVI-A	9:26	1.04	−0.40	1.12	111.2	107.5
	9:40	1.11	−0.46		9:46	1.07	−0.46	1.21	112.3	97.7
	10:00	1.14	−0.56		10:00	1.12	−0.59	1.25	116.3	100.3
	10:14	1.32	−0.74		10:16	1.33	−0.75	1.55	118.8	103.9
LASCO-C2	11:05	2.44	−1.20	COR 1A	11:05	2.52	−1.06	2.78	114.0	106.3
	11:25	2.98	−1.31	COR 2A	11:22	2.92	−1.20	3.27	112.6	99.5
	11:49	3.61	−1.53		11:52	3.67	−1.38	4.00	111.3	104.3
	12:25	4.69	−1.96		12:22	4.61	−1.71	5.10	111.1	99.7

Notes. For Y, Z, R (all in units of R_{sum}), θ, and φ (both in deg) refer to Figure 11 for explanation. Time is in UT.

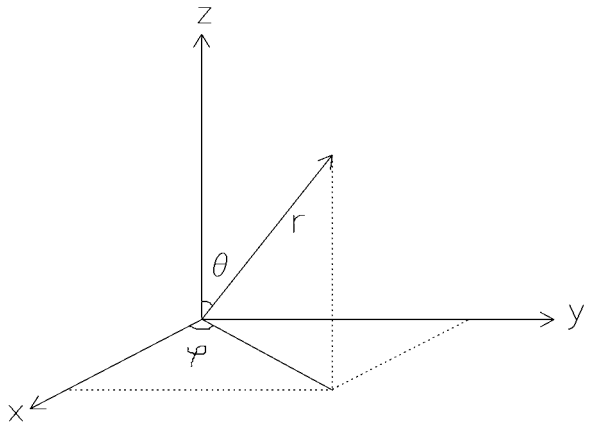

Figure 11. Coordinates for the three-dimensional reconstruction of the CME core trajectory. X is the Sun–Earth direction (positive is toward the Earth), $Y - Z$ is the *SOHO* plane of the sky, with Z pointing north and Y pointing west.

acceleration are rather uncertain. The CME front is still being accelerated when it fades away, and it has reached a velocity of $\simeq$700 km s^{-1}. The velocity difference between different parts of a CME was already noted before (for example, Webb & Jackson 1981).

3.2.3. EIS, EIT, and XRT Velocity Measurements at 1.1 Solar Radii

An independent determination of the total velocity of the CME core at 1.1 solar radii is given by the combination of measurements of plane of the sky velocity with EIT and Doppler velocities measured by EIS.

In order to measure Doppler shifts with EIS spectra, it is first necessary to correct the EIS wavelength scale for any systematic shift due to orbital motions or other effects. The EIS slit is much longer than the size of the CME ejecta, so that during the CME observations a large portion of the EIS slit observes the background active region. To correct for any instrumental systematic wavelength shift, we have measured the centroid of coronal lines in the sections of the slit above and below the CME ejecta, under the assumption that the emitting plasma was not moving along the line of sight. We have used bright lines to minimize uncertainties: Fe XII 192.39 Å, Si x 277.28 Å, and Fe XIII 202.04 Å. Their rest wavelengths were taken from the CHIANTI database, which has collected them from the literature and also gives the original sources. A systematic shift was found for each spectrum, and its magnitude increased with time from $\simeq$4 km s^{-1} in the first spectrum to $\simeq$50 km s^{-1} in the last spectrum. These shifts were removed from the centroid wavelengths measured on the CME lines before determining Doppler shifts and line-of-sight velocities for the CME ejecta.

The lines that we have used to measure the line-of-sight speed of the CME ejecta are listed in Table 4, along with the results obtained for each of the four spectra where the CME ejecta were visible. Some of the measurements have large uncertainties, but in general there is no specific trend in the results. Within each spectrum, no common velocity value can be found, except for the first one where a velocity 20–50 km s^{-1} toward the observer is measured in all ions, except the two formed at highest temperature (Si VII and Fe VIII), whose velocities are much smaller. Velocities change for each ion in the four spectra. In an approximate way, velocities within each ion tend to decrease their value and in some cases even to reverse their direction, as if the emitting material changed its direction from toward to away from the observer. However, within each ion there is considerable scatter in the velocity values and therefore no definitive conclusion can be drawn. In general, the only conclusion that can be derived from these measurements is that velocities along the line of sight are limited, and their value is less than 20 km s^{-1}, except in the first observations where they reach 20–50 km s^{-1} toward the observer.

EIT velocity measurements could be made between 9:40 UT and 10:00 UT and 10:00 UT and 10:14 UT. They too are reported in Table 4 and show a slowdown between 9:40 UT and 10:00 UT. The total velocity measurements they provide are in agreement with those obtained from geometrical considerations applied to EIT and EUVI-A images.

Average velocities in the XRT plane of the sky could be measured by comparing the position of the same feature of the CME ejecta in two subsequent images. In order to provide velocity measurements comparable to those obtained with EIS, we have calculated average velocities of features in the XRT images crossing the EIS field of view observed at approximately the same time of the beginning and the end of each EIS exposure, so that the time elapsed between two images used for velocity measurement is approximately 600 s. We measured the velocity along both the north–south and the east–west directions. The results are reported in Table 4. It is important to note that during each of the four exposures, EIS and XRT were observing a different portion of the CME core plasma than the previous exposure, so that the velocities reported in Table 4 are *local* velocities that cannot be associated with a single feature within the CME core. The XRT plasma has a more linear dynamical evolution than EIT, and only after 10:00 UT are the two plasmas showing the same velocities.

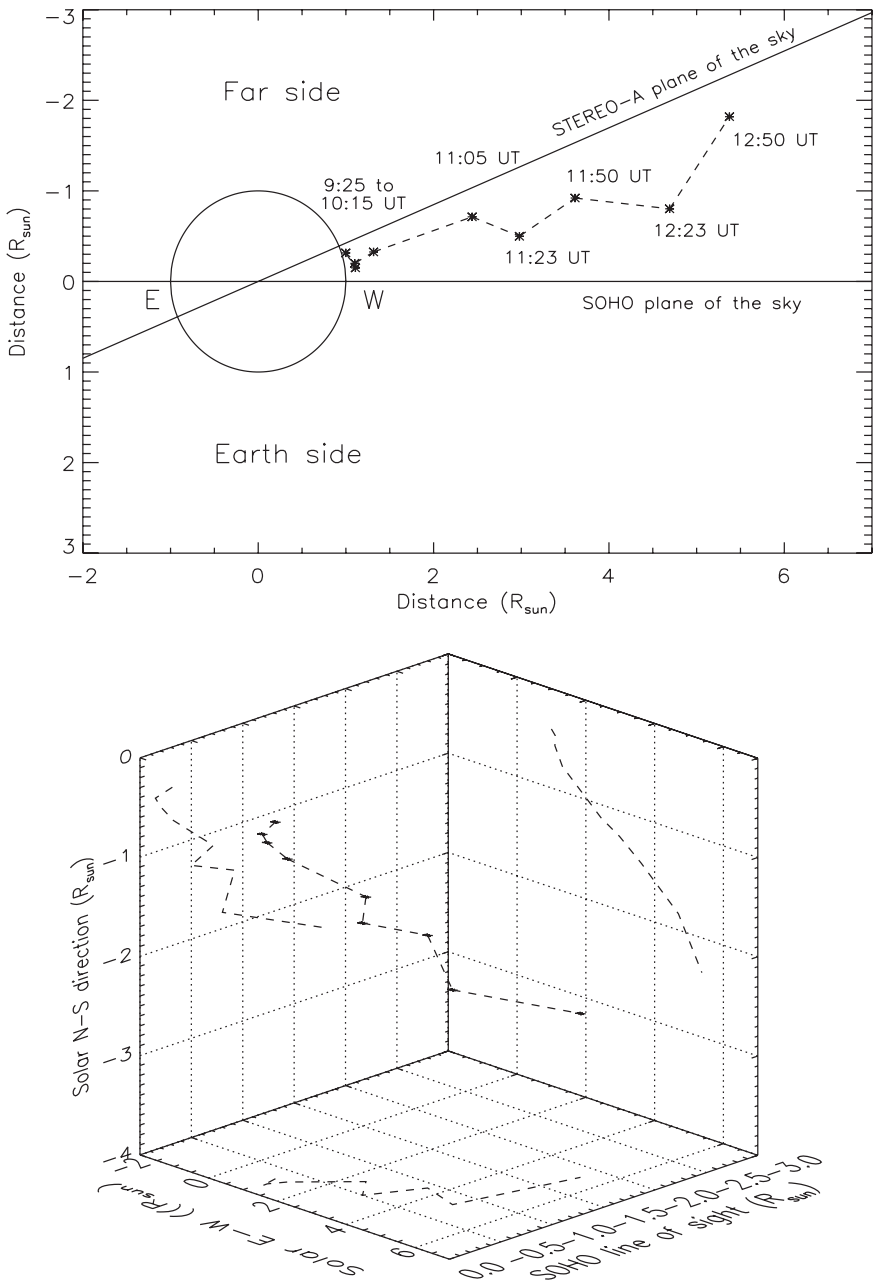

Figure 12. Top: view of the trajectory of the CME projected on the *X*–*Y* plane, as indicated in Figure 11. Bottom: CME trajectory in three dimensions.

3.2.4. UVCS and COR 1A Velocities at 1.9 Solar Radii

UVCS detected the ejected plasma near the end of the slit as bright H I Lyα emission. It was first detected at 10:35 UT, brightened by a factor of 300 over the course of 10 minutes, and spread from the end of the slit toward the center of the detector before fading away. Figure 15 shows the H I Lyα time–intensity and time–velocity of the CME as it passes through the UVCS slit. Figure 15 (left) was made in the same way as for the EIS intensity–time images. In addition, a similar image has been obtained with Doppler velocity along the slit in the place of intensity. The ejecta reached a redshift of about 70 km s^{-1} (see Figure 16). If we assume that the total velocity of the ejecta at UVCS heights is the same as at EIS heights, this implies a velocity in the plane of the sky of $\simeq$185 km s^{-1}. If the plasma, as is likely, is accelerated further, this value is only a lower limit.

To relate the observations by UVCS to those of COR 1A, we must identify features seen by both instruments. In the COR 1A image at 10:45 UT shown in Figure 2, the point farthest north in the bright rope is identified with the farthest northward excursion of bright material seen in UVCS at $Y = -634''$ at 10:48 UT. Solar north is defined by the solar pole: geometrical considerations allow us to determine that the features seen in UVCS at 1.96 $R_{\rm sun}$ appear slightly higher in COR 1A, at 2.02 $R_{\rm sun}$. This implies that the plasma lies behind the plane of the sky by about 0.5 $R_{\rm sun}$ as seen from the Earth. This distance fits in well with the results in Tables 3 and 4.

3.2.5. Acceleration

Acceleration can be measured in two ways: either using consecutive velocity measurements, or fitting a curve to the ensem-

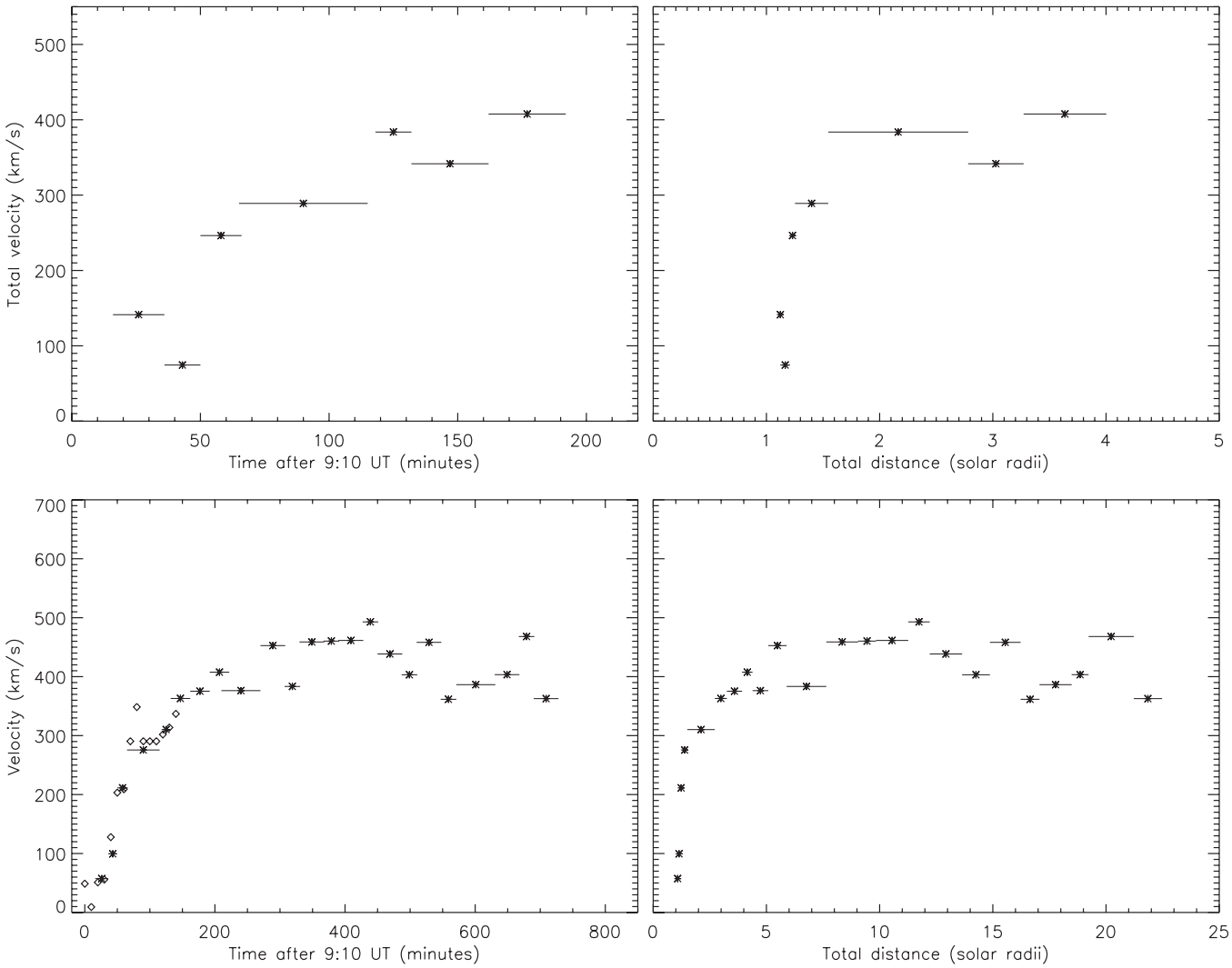

Figure 13. Top: absolute value of the total velocity of the CME core. Bottom: LASCO measurements of the CME core velocity projected on the *SOHO* plane of the sky. EUVI-A measurements are superimposed to the left panel for comparison purposes.

ble of all the velocity measurements. The first method could not be applied, because of the large uncertainties associated with each velocity measurement. The effect of such uncertainties is magnified when velocity differences are calculated from the measurements.

We have used the second method and applied it to the velocity measurements displayed in Figures 13 and 14. We measured the acceleration from the velocity of the core and of the front. The acceleration of the CME front has been determined from a linear fit of the velocities displayed in Figure 14, and it has been found to be 172 m s^{-2}. For comparison purposes, Figure 14 also displays the acceleration measured from consecutive velocity measurements, showing that it is dominated by noise and it is extremely variable.

The acceleration of the core has been first measured from the total velocity measurements. Uncertainties in the velocity measurements prevent us from measuring the vector acceleration, so we limited ourselves to fitting a straight line to the measurements shown in Figure 13 (top), obtaining an acceleration of 59.6 m s^{-2}. The velocity in the *SOHO* plane of the sky shown in Figure 13 (bottom) was broken in two parts, each fitted with a straight line: below and above 5 R_{sun}. Below this limit, the plasma is constantly accelerated, with an acceleration of 40.5 m s^{-2} (consistent with being the prejection in the *SOHO* plane of the sky of the acceleration measured from the total velocity); above this limit the plasma travels with constant velocity.

3.3. Electron Density

The electron density of the plasma along the line of sight has been determined using density sensitive line intensity ratios available in the EIS range. Most of them belong to coronal lines not involved in the CME event, so that the density of the background plasma can be measured. Some, however, belong to transition region ions, and can help determine the density of the CME core. The results are listed in Table 5.

To measure the density of the background, we have used Fe XII, Fe XIII, and Si X line intensity ratios. Their values are in agreement within uncertainties, although the Fe XII densities are slightly higher than those from the other two ions. This fact has been already noted by Young et al. (2009) and Watanabe et al. (2009), who ascribe this discrepancy to Fe XII atomic data.

The density of the CME core has been measured using O IV,V, Mg VII, and Fe VIII. To determine the true density of the CME core, it is first necessary to remove the contribution of the background plasma to the intensities of the lines of each of

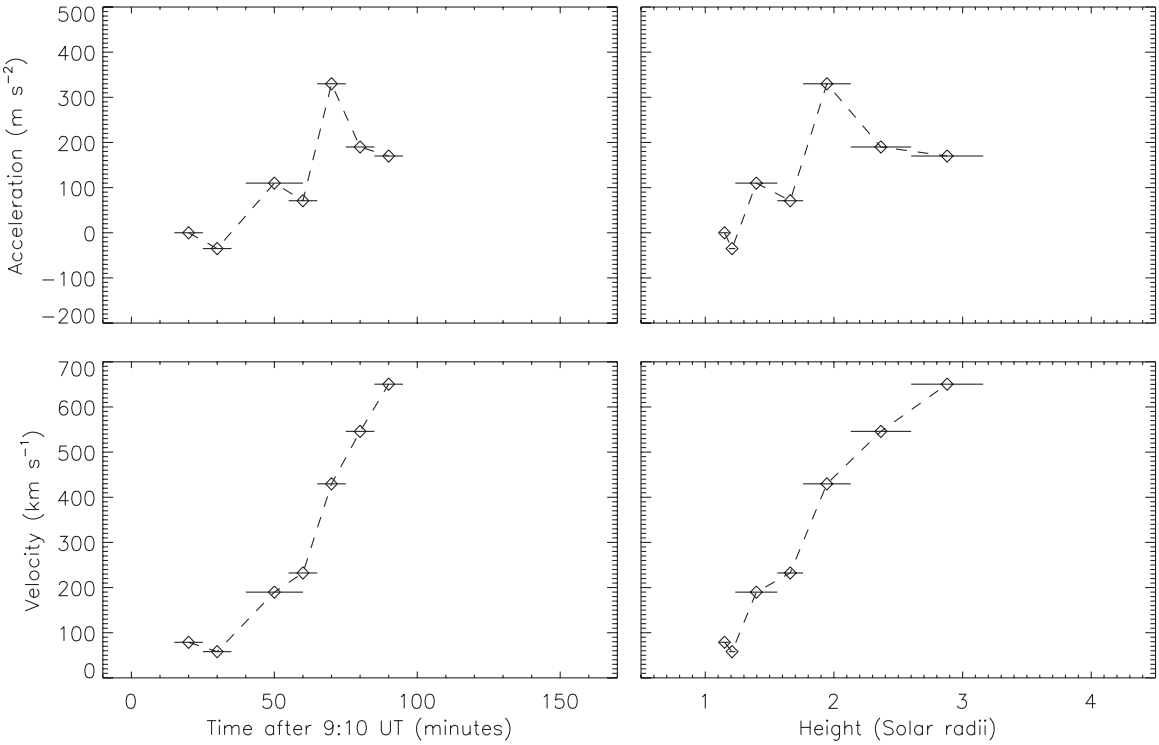

Figure 14. Velocity and acceleration of the outer front of the CME as seen by *STEREO-A*. Measurements up to 1.5 R_{sun} were made with the λ304 channel of EUVI-A, measurements made beyond 1.5 R_{sun} were made with COR 1A. The horizontal error bar in each measurement represents the 10 minute cadence of the measurements, and the corresponding range of heights in the right panel.

Table 4
Velocity Measurements in the CME Core from XRT, EIT, and EIS in km s^{-1}

Ion	Wavelength (Å)	9:30–9:40 UT	9:40–9:50 UT	9:51–10:01 UT	10:01–10:11 UT
O IV	279.93	−38.6 ± 2.1	−10.7 ± 3.2	−2.1 ± 3.2	−9.6 ± 7.5
O V	248.46	−37.4 ± 4.8	−6.0 ± 3.6	−2.4 ± 3.2	−38.6 ± 16.9
Mg V	276.58	−59.7 ± 6.5	−17.4 ± 15.2	1.1 ± 4.3	19.5 ± 11.9
Mg VI	268.99	−43.5 ± 4.5	−4.3 ± 5.4	−12.3 ± 4.5	−5.6 ± 7.8
Mg VII	276.14	−22.8 ± 4.3	−4.3 ± 5.4	−10.9 ± 4.3	−7.6 ± 8.7
Si VII	275.35	−7.6 ± 2.2	5.4 ± 9.8	9.8 ± 2.2	10.9 ± 3.3
Fe VIII	185.21	−6.5 ± 3.2	11.3 ± 1.6	6.5 ± 1.6	16.2 ± 3.2
EIS average		−30.9 ± 19.6	−3.7 ± 9.6	−1.5 ± 8.2	−2.1 ± 20.0
		9:24–9:40 UT	9:40–10:00 UT		10:00–10:14 UT
EIT (E–W)		79.8	18.0		145.2
EIT (N–S)		32.7	56.9		153.5
Total velocity		91.6	59.8		211.3
XRT (E–W)		12.7	43.1	73.1	118.4
XRT (N–S)		14.5	72.8	96.7	158.1
Height		1.10	1.11	1.13	1.17

Notes. Height is in solar radii (the photosphere being at 1 R_{sun}). Positive velocities indicate motion *away* from the observer, negative velocities indicate motion *towards* the observer. Positive velocities for XRT and EIT indicate westward motion (E-W direction) and southward motion (N-S) direction. The total velocity is the absolute value of the velocity vector.

these ions. This was done by looking at the intensity of the lines of these ions as a function of position along the slit. O IV, O V, and Mg VII were only emitted by the CME core, so no correction was necessary. Lines from Fe VIII, in contrast, were also visible outside the CME core position. We removed the background contribution by fitting the intensities of the Fe VIII lines along the slit outside the CME core with a second-order polynomial, and subtracting the resulting curve from the intensities measured inside the CME core. A similar procedure has also been applied to the Si IX lines, which are emitted both by the CME core and by the background. However, the density sensitive Si IX line at 258.08 Å turned out to be emitted almost entirely by the background, and the residual intensity due to the CME core did not allow an accurate density diagnostics.

Table 5 shows that the CME core was not homogeneous, and the value of the density depended on the temperature of the ion from which it is determined. In fact, O IV and O V line ratios provide a density more than one order of magnitude larger than the density indicated by Mg VII and Fe VIII. The latter value is larger than the density of the background plasma, but it is still

Table 5
Density Measurements Obtained from Line Intensity Ratios

Ion	Ratio	log T_{max} (K)	log N_e (cm^{-3})			
			9:30–9:40 UT	9:40–9:50 UT	9:51–10:01 UT	10:01–10:11 UT
O IV	207.2/279.6	5.18	>11.0	>11.3		
O V	192.9/248.4	5.37	$11.0^{+0.1}_{-0.2}$	$10.5^{+0.2}_{-0.3}$	$10.5^{+0.2}_{-0.3}$	<10.0
Fe VIII	185.2/186.6	5.56	$8.2^{+0.4}_{-0.25}$	$8.2^{+0.4}_{-0.25}$	$8.25^{+0.6}_{-0.3}$	8.25 ± 0.35
Mg VII	280.7/276.1	5.80	8.37 ± 0.07	8.70 ± 0.07	8.67 ± 0.06	8.95 ± 0.05
Fe XII	186.8/195.1	6.13	8.35 ± 0.07	8.42 ± 0.07	8.42 ± 0.07	8.28 ± 0.08
Si X	258.3/261.0	6.14	$8.2^{+0.15}_{-0.2}$	$8.2^{+0.15}_{-0.2}$	$8.25^{+0.15}_{-0.2}$	7.95 ± 0.35
Fe XIII	203.8/202.0	6.20	8.25 ± 0.05	8.25 ± 0.05	8.30 ± 0.05	7.75 ± 0.05

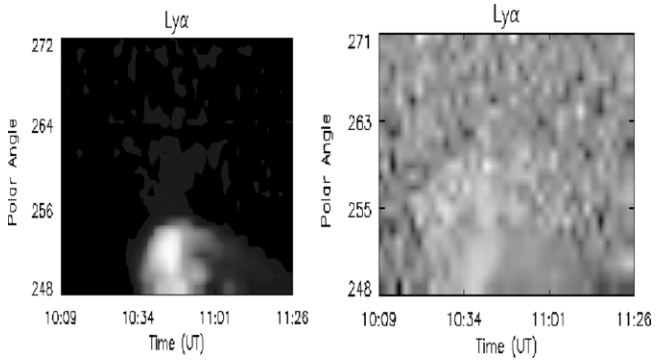

Figure 15. Time–intensity (left) and time–velocity (right) maps for UVCS H I Ly α observations.

comparable to it. This seems to indicate that ions formed in different temperature ranges were emitted by different plasma elements.

3.4. Thermal Structure

The thermal structure of a multithermal plasma is usually described by the differential emission measure (DEM) $\varphi(T) = N_e^2 \times dV/dT$, where V is the plasma volume and T is its temperature. The DEM is used to indicate the distribution of the amount of plasma as a function of temperature. We have determined the DEM of the CME core by using the iterative DEM diagnostic technique developed by Landi & Landini (1997), using all the lines available in each data set. The background emission has not been removed from the lines emitted by the CME core for two main reasons. First, it was rather difficult to do for both the weakest lines in the data set, and for those lines where the CME core provided only a small component of the total intensity. Second, we were also interested in the DEM distribution of the background plasma itself, to investigate how the background plasma reacts to the CME.

The DEM was determined for each of the EIS exposures where the cores were observed, corresponding to four different positions along the slit, selected following the CME core: we averaged EIS emission over pixels 240–320 (spectrum 1), pixels 190–300 (spectrum 2), pixels 140–250 (spectrum 3) and pixels 100–180 (spectrum 4). For comparison purposes, the DEM of the emitting plasma was also measured before and after the CME event, averaging the emission over the same pixels of the closest CME data set: pixels 240–320 (before the event) and pixels 100–180 (after the event).

The lines that we have used for the DEM determination, as well as their intensities, are reported in Table 6. These include the He II 256.317 Å line intensity, as well as the intensity of the continuum between 190 Å and 200 Å. He II line formation in disk spectra is usually more complex than the simple collisional-radiative model sufficient for all other lines and it is not yet fully understood (e.g., Andretta & Jones 1997, and references therein). However, disk emission was seen by an outward moving CME plasma to be sufficiently redshifted to effectively suppress self-absorption, so that He II emission could be safely modeled using the collisional-radiative model. Using this approximation, we have used the He II line at 256.317 Å to constrain the DEM at the lowest end of the temperature range, after subtracting the coronal contribution of a blending Si X line from the observed intensity of the 256.3 Å feature using the Si X branching ratio $\lambda 256.37/\lambda 261.04$.

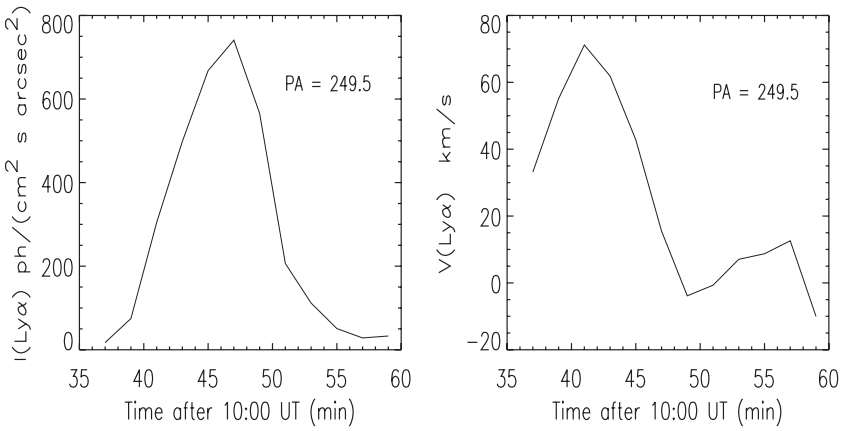

Figure 16. H I Lyα intensity (left) and velocity centroid (right) as a function of time, measured from a 28″ long portion of the UVCS slit at P.A. = 249°.5.

Table 6
Observed Intensities of the Lines Used in the DEM Reconstruction

Ion	λ (Å)		Spectrum 1	Spectrum 2	Spectrum 3	Spectrum 4	
		9:20–9:30UT	9:30–9:40UT	9:40–9:50UT	9:50–10:00UT	10:00–10:10UT	10:10–10:20UT
Continuum			1.2	1.6	1.9	0.7	
He II	256.317		57.6	71.8	71.3	36.1	
O IV	207.239		1.2	1.4			
O IV	279.631		2.0	2.1	1.9	1.4	
O IV	279.933		4.0	4.6	5.3	2.1	
O V	192.904		7.5	6.9	7.9	2.6	
O V	248.460		6.4	8.0	9.2	4.4	
Mg V	276.579	0.8	1.0	1.6	2.3	0.6	1.9
Mg VI	268.991	0.3	0.9	1.6	2.3	0.7	
Mg VI	270.391	0.3	2.1	3.5	5.0	1.9	0.2
Mg VII	276.138		1.1	1.4	2.3	0.8	
Mg VII	280.745		0.6	1.1	1.8	1.0	
Al VIII	250.139	1.0	1.0	1.1	1.5		
Al IX	282.421		1.5	1.1	1.37	0.4	0.7
Al IX	284.025		4.6	3.5	3.7	2.7	
Si VI	246.003		2.6	3.2	5.2	1.8	
Si VI	249.124		1.1	1.3	1.2	1.8	
Si VII	272.639		1.5	2.7	3.5	1.5	
Si VII	275.354		6.8	9.0	11.9	5.0	
Si VII	275.668		1.1	1.4	2.0	0.9	
Si IX	258.082		0.7	1.3	1.5		0.3
Si IX	290.687		5.2	4.3	3.8	1.9	
Si X	253.788		3.8	3.1	2.3	2.4	0.7
Si X	258.371		19.8	15.1	10.6	5.1	3.9
Si X	261.044		13.4	10.3	7.1	3.9	
Si X	272.006	12.8	13.3	10.6	6.8	4.5	0.4
Si X	277.278		9.2	7.4	5.8	2.6	
S X	257.147		3.9	3.1	21.8	10.1	6.4
S X	259.497		7.1	5.4	3.8	2.0	2.3
S X	264.231		8.3	6.5	5.0	3.1	1.9
Fe VIII	185.213	4.4	9.2	11.9	16.7	6.2	1.9
Fe VIII	186.599	3.5	7.3	9.5	13.0	5.1	1.5
Fe VIII	194.661	1.4	2.6	3.3	4.6	1.8	0.5
Fe IX	171.073	198.8	219.8	214.6	207.7	86.0	
Fe X	174.531	109.3	111.2	88.6	75.1	34.6	25.5
Fe X	175.263	11.1	6.7	5.8	10.4	7.5	
Fe X	177.240	58.1	54.4	45.9	40.2	19.7	12.1
Fe X	184.537	26.1	25.4	21.4	19.0	9.6	6.3
Fe X	190.037	10.3	10.1	8.0	6.4	3.3	2.3
Fe XI	180.408	99.1	94.5	74.4	57.2	29.7	23.9
Fe XI	182.169	11.4	11.7	9.1	7.2	3.2	2.4
Fe XI	188.232	50.0	46.9	38.4	26.1	13.1	9.0
Fe XI	188.299	34.3	34.1	26.5	19.7	8.2	6.2
Fe XI	192.830	13.5	11.0	11.6	9.4	4.5	2.7
Fe XII	186.887	8.4	9.2	7.3	5.5	2.4	1.3
Fe XII	192.394	22.0	19.5	15.7	11.8	6.2	4.6
Fe XII	193.509	45.0	44.3	37.5	27.6	14.9	10.9
Fe XII	195.119	81.9	81.4	59.9	45.3	23.6	17.5
Fe XIII	200.022		3.6	2.7	2.1		0.5
Fe XIII	201.128		14.4	11.2	8.7	4.5	3.0
Fe XIII	202.044		64.5	48.3	36.3	21.1	15.0
Fe XIII	203.164		1.9	1.2	1.1	0.3	
Fe XIII	203.828		10.6	8.2	6.7	1.2	1.6
Fe XIII	204.263		2.0	1.3	1.2	0.5	0.4
Fe XIII	204.945		4.3	4.1	3.6	1.7	
Fe XIII	209.919		8.8	7.6	5.0	3.5	3.2
Fe XIV	211.318		26.3	20.0	18.7	9.6	7.1
Fe XIV	264.790		9.9	8.0	6.5	3.5	2.0
Fe XIV	270.522	4.5	4.8	4.1	3.5	2.2	1.2
Fe XIV	274.204	12.7	14.0	12.0	10.7	5.7	
Fe XV	284.163		33.1	31.8	27.8	17.2	9.4

Notes. Line intensities are in photon cm^{-2} s^{-1} $arcsec^{-2}$, the continuum intensities are in photon cm^{-2} s^{-1} $arcsec^{-2}$ $Å^{-1}$, and have been averaged in the 190–200 Å wavelength range. The times (in UT) in each column correspond to the beginning and end of the EIS integration time: 9:20–9:30 UT corresponds to the observation immediately *before* the appearance of the CME ejecta in the EIS field of view; 10:10–10:20 UT corresponds to the observation immediately *after* the CME disappearance.

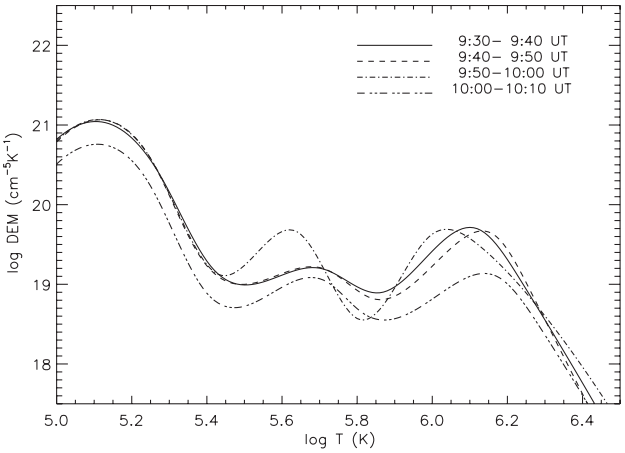

Figure 17. DEM distributions of the CME core as a function of time, in the four spectra where the core was visible.

We also have used the intensity of the continuum observed in the EIS short wavelength channel. That continuum emission is best observed between 190 Å and 200 Å, where the EIS reflectivity is largest. We measured the continuum intensity in four small wavelength ranges free of line emission (190.52–190.75 Å, 196.25–196.34 Å, 197.680–197.72, and 201.27–201.44 Å) and averaged the results; in that wavelength range, continuum emission is expected to change by less than 25% for temperatures larger than 10^5 K, less than the measured uncertainties. Attempts at measuring the continuum in the EIS long wavelength channel failed, as no appreciable emission was measurable. The Fe XVI 262.9 Å and Fe XVII 204.6 Å lines shown in Figure 8 are very faint and their intensities are too low to be used reliably for DEM determination.

The resulting DEM distributions are displayed in Figure 17. The DEM curves show three distinct features that dominate the emission at three different temperature regimes. At very low temperature ($\log T \simeq 5.1$) there is a first maximum; at lower temperatures, the DEM is mostly due to extrapolation and therefore has no real physical meaning. This maximum is determined by the lines of He II, O IV, O V, and Mg V, and by the continuum. This feature has the same temperature distribution in all four EIS spectra, but it decreases the DEM value in the last one. At higher temperatures the DEM drops by more than two orders of magnitude indicating that very little plasma connects it with the second feature common to all the DEM curves of the CME core: a peak at $\log T \simeq 5.6$–5.7. This latter feature has a lower DEM than the colder one, and its DEM value changes with time, being maximum in the third spectrum. In the last spectrum, it behaves like the colder feature by decreasing its DEM value. This feature is determined by the ions Mg VI-VII, Si VI-VII, and Fe VIII. The third feature peaks at $\log T \simeq 6.1$, it is remarkably constant in the first three spectra, and it lowers its DEM value (but not its temperature) in the last data set; it is determined by Fe IX-XV, Si IX-X, and S X.

By inspecting Figure 17 we can conclude that during the entire observation, the CME core thermal distribution shows no change except in the DEM value of the second peak at around $\log T \simeq 5.75$ between 9:50 UT and 10:00 UT. It is interesting to note that the temperatures of the two cold peaks in the CME DEM correspond to the two temperature ranges where line ratios provided two different values of electron density. This most likely means that the CME core is made of two components traveling together: a cold and dense one ($\log T \simeq 5.1$, $\log N_e \simeq 10$–11) and a hotter and less dense one ($\log T \simeq 5.7$, $\log N_e \simeq 8.7$). These two separate components were observed in other events with C III and O VI lines, and found to have different size and shape (Kohl et al. 2006).

The peak at coronal temperatures is due to background plasma. Figure 18 shows the DEM curves of the CME core during the first (left) and last (right) EIS spectra where the core was visible. Superimposed to the two curves are the DEM curves determined from the emission observed at the same location as the core, just before (left) and after (right) the CME event. These "background" DEM curves have the standard shape for off-disk plasmas, with a peak slightly above 1 MK. The peaks of these curves are almost identical to the highest temperature peaks measured during the CME event, indicating that the CME core does not produce significant emission at coronal temperatures. The lack of reliable constraints on the upper transition region DEM of the background plasma makes it difficult to estimate to what extent the background contaminates the CME core DEM

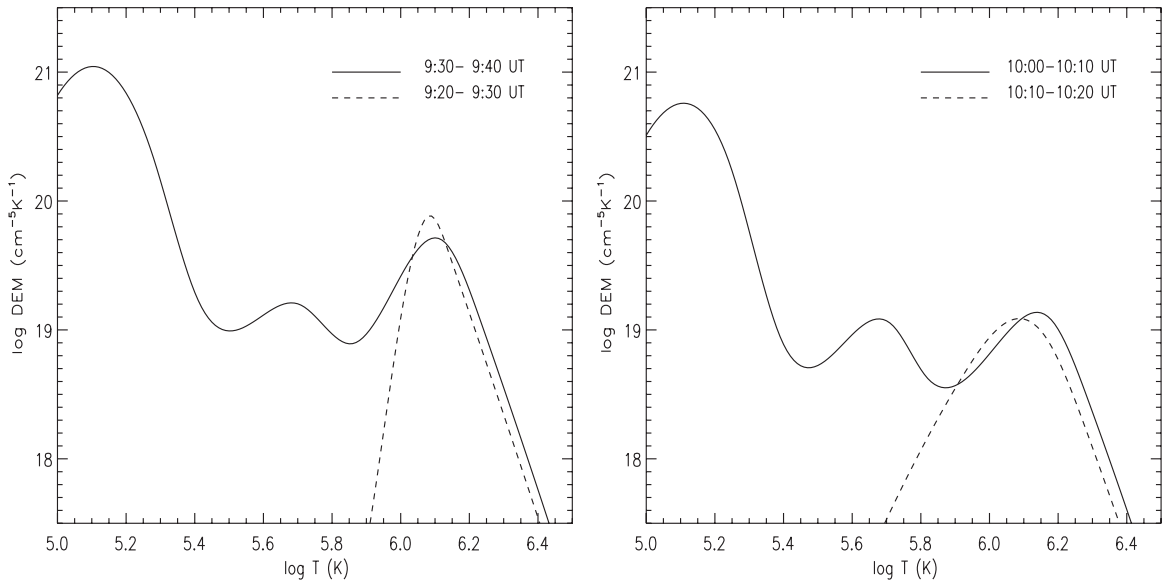

Figure 18. Comparison of the DEM distribution of the CME core (full line) with the background (dashed line) before (left panel) and after (right panel) the CME event.

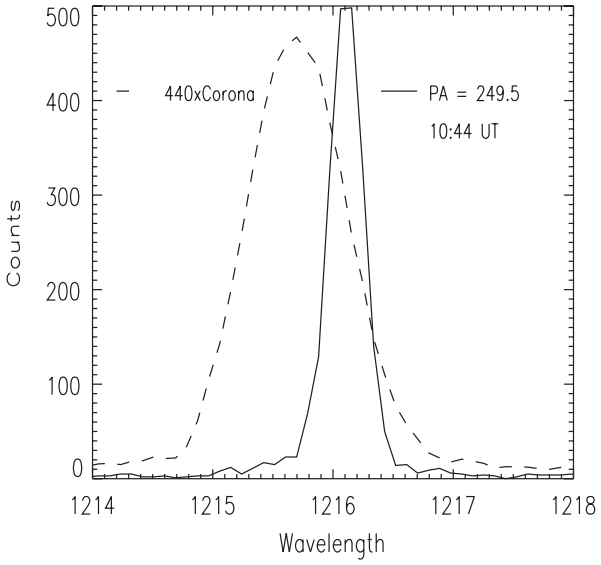

Figure 19. H I Lyα line profile. The dashed line is the pre-CME coronal profile multiplied by 440, while the solid line shows the profile from a 28″ long portion of the UVCS slit in the exposure at 10:44 UT.

curves at the temperatures of the two cooler peaks. Also, the absolute value of the peak of the coronal DEM has decreased after the CME event. Since the electron density is the same, the likely explanation is that probably the CME event has swept away part of the coronal material in the EIS field of view.

Constraints on the plasma temperature of the core at UVCS heights can be inferred from the H I Ly α intensity and line width. The $1/e$ line width of about 25 km s^{-1} (Figure 19) indicates temperatures below 40,000 K. The outflow speed of 225 km s^{-1} (Section 4.2) means that radiative scattering makes little contribution to the H I Ly α intensity. Collisional excitation must generate the H I Ly α emission, and that requires temperatures of at least 15,000 K for the electron column density obtained in Section 4.2. This range of temperatures is below the one accessible with EIS spectra, but the gas may have cooled as it traveled from 1.1 to 1.9 solar radii.

3.5. Filling Factor and Mass

Since the *SOHO*/*Hinode* and *STEREO-A* satellites observed the Sun from two different points of view, we can use EUVI-A images to provide an upper limit to the length of the CME core along the *SOHO*/*Hinode* line of sight using simple geometrical arguments. That quantity can be used for two purposes. First, when combined with the knowledge of the emission measure of each plasma component, it can provide the filling factor of the plasma. Second, it can also be used to determine an upper limit to the CME core volume, that can be combined with the plasma electron density and filling factor to determine the mass of each component of the CME core.

We used EUVI-A and EIT images at 10:00 UT to determine the length L of the CME core along the EIT line of sight and found $L \leqslant 1.70 \times 10^{10}$ cm. A lower limit of L cannot be determined, by we assumed the linear dimension of the CME in the EIS field of view to be a reasonable estimate of it: $L \simeq 8.7 \times 10^{9}$ cm. We then integrated the DEM determined in the previous section over temperature to obtain the emission measure (EM) for the cold and the transition region components of the CME core. We integrated the DEM in the $\log T = 4.9$–5.4 and $\log T = 5.5$–5.9 for the cold (C) and the transition region (TR) components, respectively, and found $\mathrm{EM_C} = 3.26 \times 10^{25}$ and $\mathrm{EM_{TR}} = 2.20 \times 10^{24}$ cm. This allowed us to determine the electron density of the two plasmas from the emission measure definition $\mathrm{EM} = N_e^2 L$ and comparison with line ratios yielded the filling factors f for the two core components to be $f_\mathrm{C} = (1.5$–$2.1) \times 10^{-3}$ and $f_\mathrm{TR} = (2.3$–$3.2) \times 10^{-2}$.

EIT images show that the CME core covered an area $A \simeq 2.4 \times 10^{20}$ cm^2, so that the volume is $V = (1.9$–$4.0) \times 10^{30}$ cm^3. Considering that the plasma was completely ionized, and using the electron density estimates for the cold and TR portions of the CME core, the masses of the two components were in the range $M_\mathrm{C} = (1.4$–$3.2) \times 10^{14}$ g and $M_\mathrm{TR} = (3.5$–$7.7) \times 10^{13}$ g. The total mass was thus $M = (1.8$–$4.0) \times 10^{14}$ g. These values are in line with estimates obtained from other instruments and other techniques. Also, they show that the TR component of the core is less dense, lighter, and less filamentary than that of the core, even though it still remains highly structured below the resolution of all instruments (ranging between 1″ and 6″).

In addition to the cool gas discussed above, there is the hot component seen with XRT. Since we do not have accurate estimates of the density, temperature and emission measure of the XRT plasma, we can only provide a very rough estimate for its mass. In Section 3.6, we find that this gas has a total emission measure of around 2×10^{25} cm^{-3}; XRT images suggest a length scale of order 1.5×10^{10} cm. If the gas is evenly distributed, the average density is 4×10^{7} cm^{-3} and the mass is 3×10^{14} g, comparable to the total mass of the core.

3.6. The XRT Emission Feature

The nature of the plasma that produces the XRT emission, and its relation to the CME core needs to be investigated. Figure 7 shows that the XRT emission envelops the CME core; if we combine this with the three-dimensional trajectory shown in Figure 12, we can conclude that the CME core was preceding the XRT plasma, and that the latter enveloped its tail like a cup. A similar conclusion can be drawn if the time–intensity plot built from the XRT images at the location of the EIS slit is compared to the EIS time–intensity image of the CME core. Such a comparison is displayed in Figure 20. This figure shows an intensity–time plot obtained by lining side by side the portions of the XRT images that correspond to the field of view of the EIS slit: in the left panel, the original time resolution of XRT (1 minute) is maintained; in the right panel, the EIT emission is rebinned to simulate the EIS time resolution (10 minutes). The He II emission is overlaid to the XRT image after a careful check of the relative pointing of EIS and XRT. Figure 20 clearly shows that the XRT emission *trailed* the CME core emission as observed by EIS. After the CME event, the XRT intensity increased at the same position where the Fe XV emission brightened. This means that even if the XRT initial brightening was tied to the CME event, it was likely not due to the cold material seen by EIS.

In order to investigate the nature of the XRT emission, we have used the EIS DEM curves shown in Figures 17 and 18 and the CHIANTI database to calculate the expected spectrum emitted by the CME core and by the background active region in the 1–200 Å range. We then convolved the results with the XRT Al-poly spectral response function to (1) calculate the expected XRT count rates and (2) understand where the emission observed by XRT came from. This procedure is vulnerable to two sources of uncertainty.

First, a direct comparison is dependent on any systematic differences between intensity calibration of the two instruments,

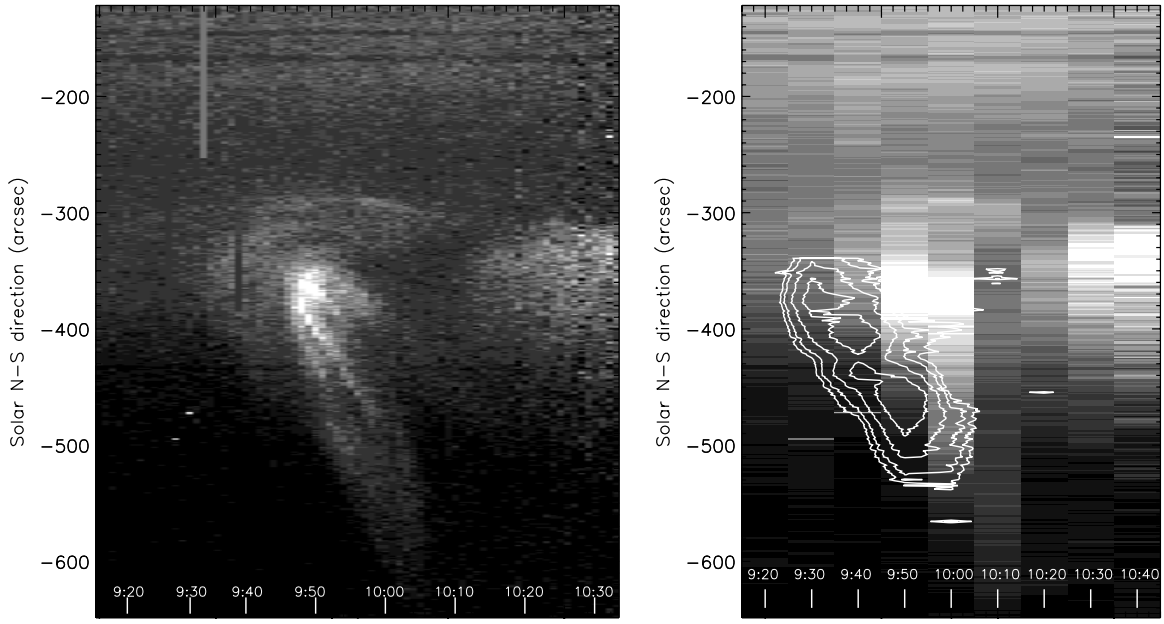

Figure 20. *Hinode*/XRT time–intensity maps of the portion of the XRT field of view corresponding to the EIS slit as shown in Figure 1. Left: original XRT time resolution; right: XRT emission rebinned to simulate the EIS time resolution. The He II 256.317 Å line emission from the CME ejecta is superimposed for comparison purposes.

Table 7
Percent Contribution of Line and Continuum Emission to the Predicted XRT Count Rates for Each Temperature Bin

log T Range	Line	Continuum			Total
		Freefree	Freebound	Two-photon	
5.1–5.2	4.27	0.02	0.41	0.32	5.01
5.2–5.3	2.59	0.02	0.21	0.09	2.90
5.7–5.8	1.45	0.01	0.03	0.00	1.49
5.9–6.0	0.00	0.14	0.70	0.20	1.04
6.0–6.1	28.26	1.06	5.32	1.67	36.31
6.1–6.2	0.00	1.05	4.98	1.68	7.70
6.2–6.3	21.36	1.18	5.11	1.77	29.43
6.3–6.4	4.17	0.79	2.95	0.98	8.89
6.4–6.5	2.63	0.41	1.19	0.35	4.58
Total cont.		4.68	20.90	7.06	
Total	64.73		32.64		

Notes. Predicted line and continuum emission were convolved with the Al-poly filter spectral response function before determining the results. Temperature bins where the contributions of all components were smaller than 1% have been omitted.

which has not been yet thoroughly checked by the EIS and XRT teams as of the time of writing. Second, the Al-Poly response function was retrieved using the standard XRT software available in *SolarSoft*, but such spectral response function (as of 2009 August) takes into account contamination on the detector, but not on the Al-poly filter itself. It is difficult to estimate a priori the effect of such contamination, as it may affect both the absolute value of the transmissivity of the filter and its wavelength dependence. In what follows, we will ignore this additional contamination, but the results we obtain need to be confirmed and validated after the filter contamination correction is made available by the XRT team.

The EIS DEM curves measured *before* the CME event were found to account only for 20%–30% of the total emission observed by XRT at the same time and place. The emission contributing to the XRT counts is reported in Table 7, where we have omitted the temperature ranges where all individual contributions were smaller than 1%. Continuum radiation (mostly free-bound radiation) accounts for $\simeq$30% of the predicted XRT counts, the rest being provided by spectral lines. The dominant line emission comes from O VII lines around 21–22 Å, from C V,VI emission in the 30–40 Å range, and from coronal emission in the 170–190 Å range. We repeated the exercise using one of the CME DEM curves, finding that the cold material responsible for the CME emission in the EIS spectra only provides a negligible contribution to the XRT emission: only the background coronal plasma is predicted to contribute to the XRT images.

The discrepancy between the predicted count rates in the background plasma may be due to calibration issues, but calibration cannot account for the XRT emission feature related to the CME. The bright XRT feature trailing the CME core was observed in a region where the EIS spectral lines either were unchanged or had decreased their intensity: this means that some additional plasma must have been emitting the excess XRT counts, that EIS could not see.

Since the XRT bright feature is not emitted by the background corona at $\simeq$1 MK, there are two other possible sources for the XRT feature: cold lines emission not included in the CHIANTI database or (2) emission from plasmas hotter than $\simeq 3 \times 10^6$ K, the temperature of formation of the hottest line seen by EIS in this data set.

The presence of cold plasma can be ruled out on grounds that the XRT feature is not co-spatial with the CME core. But even if the two plasmas were cospatial, cold material cannot be responsible for the XRT bright emission, because the wavelengths of the emission lines that CHIANTI does not include lie in the 50–170 Å range, where the XRT effective area is very small. Also, any leak of longer wavelength emission in the Al-poly filter is unlikely to happen, since this leak needs to be very large. For example, the very strong He II Lyα at 303.76 Å, which is predicted to dominate the spectrum of the CME core, only provides 4% of the observed XRT counts if we assume a response function at 303 Å equal to the 1 at 200 Å.

Table 8
Parameters of the Gaussian DEM Curves.

Quantity	Plasma Parameters		
$\log T$	6.8	6.9	7.0
$\log DEM$	19.30	19.15	19.05
σ	0.05	0.05	0.05

Note. log temperature (K) and DEM (cm^{-5} K^{-1}) of the peak, and Gaussian width σ for nearly isothermal plasmas providing the XRT missing counts, and spectra compatible with EIS observations.

The presence of additional hot plasma undetected by EIS can be tested by calculating the line and continuum contribution of a nearly isothermal plasma at temperatures larger than $\log T = 6.5$. The isothermal plasma was modeled with a Gaussian DEM, centered around a temperature $\log T_{max}$ and with a width $\sigma = 0.05$, with coronal abundances. The peak of the DEM was arbitrarily chosen to be log DEM = 21.0 cm^{-5} K^{-1}. We used this DEM to calculate the synthetic spectrum in the 1–200 Å range, and then we convolved the results with the Al-poly spectral response function. The resulting count rates were compared with the observed ones to determine the scaling factor of the DEM peak that allowed the predicted count rates to match observations. The resulting DEM was used to calculate the EIS spectra that were compared to EIS observations. We focused on a few bright lines and on the continuum in both EIS wavelength ranges. One of the lines we considered (Fe XV 284.16 Å) was actually observed by EIS, while the others (Fe XVI 262.99 Å, Ca XVI 208.60 Å, Ca XVII 192.85 Å, Fe XVII 204.67 Å, Fe XVIII 203.52 Å, Fe XXIII 263.77 Å, and Fe XXIV 192.03 Å) either have not been observed or were at the limit of detectability: we have used the intensity of the weakest lines observed by EIS ($\simeq$0.1 photon cm^{-2} s^{-1} $arcsec^{-2}$) as the upper limit for the allowed predicted intensity. We repeated this procedure choosing a grid of values for the DEM peak temperature: $\log T_{max} = 6.6$–7.2 in steps of $\Delta \log T = 0.1$.

We found that the DEM curves with $\log T_{max} = 6.6$ and 6.7 that accounted for the XRT missing counts provided a contribution to the Fe XVI 262.99 Å line that was in excess of the minimum observable EIS flux, while those with $\log T_{max} = 7.1$ and 7.2 predicted the undetected Fe XXIV 192.03 Å line to be observable in the EIS-SW band. The DEM characterized by $\log T_{max} = 6.8$–7.0 predicted line and continuum emission below the detection threshold, so that they were compatible with both XRT and EIS observations. This means that limited amounts of hot plasma at sub-flare temperature were responsible for the XRT emission feature and still were invisible to EIS. The temperature and peak DEM values that were compatible with both EIS and XRT observations are shown in Table 8.

It is important to note that these quantitative results are affected by uncertainties due (1) to the unavailability of the correction for the Al-poly filter contamination, which is still being evaluated by the XRT team and (2) to the relative EIS-XRT calibration. However, we can confidently conclude that the EIS DEM curves underestimate the count rates in the XRT Al-poly filter, and that the missing X-ray flux can only come from plasmas at temperatures higher than the EIS range in the gap of EIS sensitivity at $\log T = 6.8$–7.0.

4. HEATING OF THE CME CORE

Several independent lines of evidence indicate that CME ejecta are strongly heated well after the initial eruption. Akmal et al. (2001), Ciaravella et al. (2001), Bemporad et al. (2007), and Lee et al. (2009) used the temperatures, densities, and ionization states derived from UVCS spectra, together with models of the heating, cooling, and time-dependent ionization state for grids of different initial conditions, to show that the integrated heating was comparable to the kinetic energy for several CMEs. Rakowski et al. (2007) combined the ionization states measured at 1 AU with *ACE* with models of ionization freeze-in in the expanding ejecta, and they obtained similar results. Filippov & Koutchmy (2002) studied the transition from absorption to emission in rising filaments seen in EUV images.

Several mechanisms could heat the ejecta as they rise from heliocentric distances of ~ 1.1 R_{sun} to $\sim$2–3 R_{sun}. Wave heating similar to that in coronal holes must be present, though it would have to be a few orders of magnitude more intense to account for some of the observations (Akmal et al. 2001). Plasma rising in a twisted flux rope will tend to fall toward the bottoms of the coils, possibly generating shocks that can heat the plasma (Filippov & Koutchmy 2002). Thermal conduction could carry energy from hot plasma in the low corona, though the low temperatures and large length scales of some ejected filaments make this difficult. Another heat source is the substantial amount of magnetic energy that must be dissipated during the CME expansion (Kumar & Rust 1996; Lynch et al. 2004), though neither the dissipation mechanism nor the amount of energy available is clear. Finally, a great deal of energy is liberated in the current sheet that extends from the flare loops to the CME core. The kinetic energy of the current sheet outflow can drive slow mode shocks that work their way into the CME core (Lin 2004; Shiota et al. 2005), or the reconnection might drive wave heating or energetic particle fluxes that could heat the CME gas. One limitation of this mechanism is that strong reconnection occurs only for a relatively short time corresponding to the flare impulsive phase.

Overall, these investigations indicate that heating of the ejecta is a significant term in the energy budget of CMEs, though it is often ignored in theoretical models. The *Hinode*, *STEREO-A*, and *SOHO* observations of the 2008 April 9 CME allow us to estimate the heating in two different height ranges. First, we discuss the heating up to the position of the EIS slit, about 1.1 R_{sun} above the surface, and second we discuss the heating of material moving from the EIS slit to the UVCS slit at 1.9 R_{sun}.

The energetics of the event are summarized in Table 9. In this table, we have assumed a 10% He abundance. For the plasma at UVCS heights, we do not have a measurement for the electron density, so we assumed it to be the density of the coldest component of the CME core seen by EIS, decreased by either the expansion of the length of the structure, or by expansion for both length and radius. This estimate, however, is very crude. The thermal energy of the hot component of the CME core studied with XRT is also uncertain, due to the great uncertainty in the temperature of that component provided by the unaccounted for contamination on the Al-poly filter.

4.1. Heating at Low Heights

EIS observed emission with a DEM peaking at $\log T = 5.1$, and EUVI-A and EIT images show that this material was just completing the transition from absorption to emission. In other words, the gas was heated from temperatures below 10^4 K to (1–2) $\times$ 10^5 K. This implies an addition of heat of 3/2 times 10 eV per particle or, since the gas is ionized, 30 eV per proton.

Table 9
Energy Budget of the CME Core at 1.1 and 1.9 Solar Radii

Parameter	1.1 R_{sun}			1.9 R_{sun}
log T	5.1	5.7	6.8	4.2–4.6
log N_e	10.5	8.7	7.6	9.8–10.3
Velocity	100	100	100	290
Kinetic energy	67.7	67.7	67.7	570
Gravitational energy	2350	2350	2350	1350
Thermal energy	55.7	158	1719	16–24
Cooling time	3.2	1190	669000	>2–17
Cumulative heating	6000	80	1.5	<1440

Notes. He abundance was assumed to be 10%. The plasma electron density at 1.9 solar radii has been assumed to be the density at 1.1 solar radii, decreased by the effects either of linear expansion, or expansion of the ejecta's length and radius. Energy is in eV per particle; velocity is in km s^{-1}, the cooling time is in seconds.

The ionization of H and He requires an additional 21 eV per proton, for a total of 51 eV per proton. This heat is only a small fraction of what is really needed, however, because the heating must at least balance radiative cooling. The cooling time is $3kT/n_e\Lambda(T)$, where k is the Boltzmann constant and Λ is the cooling coefficient (e.g., Raymond et al. 1976). For the typical density of 3×10^{10} cm^{-3} measured by EIS, the cooling time is about 3 s. The characteristic timescale for expansion is, conservatively, 200 times this long, so that the total heating must be of order 6000 eV per proton or 6×10^{15} erg g^{-1}.

This heating rate can be compared with expectations based on some of the proposed heating mechanisms. The shocks discussed by Filippov & Koutchmy (2002) convert a fraction of the CME kinetic energy into thermal energy, but since the heat is much larger than the kinetic energy corresponding to the 100 kms^{-1} speed at that height (Table 4), the Filippov & Koutchmy mechanism fails to account for the heating in this CME.

The cooling rate, and therefore the minimum heating rate, corresponds to 0.6 erg cm^{-3} s^{-1}. This is around 10^5 times larger than the wave heating near the base of a coronal hole (e.g., Allen et al. 1998). While a relatively large heating rate might conceivably occur above an erupting active region, it would require wave amplitudes of hundreds of kilometers per second, and they are not seen as Doppler broadening in the EIS spectra.

Thermal conduction is also problematic as a heating mechanism. Assuming that the long filaments seen in COR 1A and EUVI-A correspond to magnetic field lines, and that conduction across the field is strongly suppressed, the conductive heating rate for $T \sim 10^{5.1}$ and a length scale of 10^{10} cm is about 0.02 erg cm^{-3} s^{-1}. Thus thermal conduction also fails to account for the heating.

In addition to the cool gas discussed above, there is the hot component seen with XRT. It takes 50 times more energy per particle to produce the hot component, but the radiative cooling rate is negligible, so the heating per particle is smaller than for the cool component. Moreover, the mass in the hot component is two orders of magnitude larger. This estimate assumes that the hot gas is uniformly distributed, however, and if it is highly clumpy or filamentary on small scales, like the CME core plasma, the mass would be overestimated.

It is more difficult to obtain estimates for magnetic and reconnection heating rates. We will consider these mechanisms after obtaining constraints on the heating in the region between the EIS and UVCS slits.

4.2. Heating at Larger Heights

We follow the general procedure of Akmal et al. (2001) to determine the heating between the time the plasma crossed the EIS slit and the time it crossed the UVCS slit. We determine the velocity of the plasma every 10 minutes and construct grids of models with different heating rates that match the initial conditions at the EIS slit and the observed H I Lyα emission and COR 1A pB at the UVCS slit.

The plasma accelerates from $\simeq$85 km s^{-1} at the EIS slit to $\simeq$225 km s^{-1} at the height of UVCS. From the COR 1A image at 10:45 UT, the electron column density is 4.0×10^{17} cm^{-2} in the region where H I Lyα is bright in the UVCS spectra nearest that time. The H I Lyα intensity in one 28″ bin along the slit averaged over two exposures is 350 photon cm^{-2} s^{-1} $arcsec^{-2}$, and the temperature is below 40,000 K based on the line width. Based on the EIS data, we take an initial density of 3×10^{10} cm^{-3} and initial temperatures between $10^{4.8}$ and $10^{5.4}$ K.

We parameterized the functional form of the heating rate in several different ways, multiplying by a range of scale factors to determine the acceptable range of heating rates. Wave heating was modeled with an exponential dropoff with height taken from Allen et al. (1998). Heating proportional to density and to density squared were also used. Finally, in order to approximate magnetic heating due to relaxation of the flux rope, we used a heating rate proportional to the rate of increase of kinetic plus gravitational energy. This is motivated by the expanding flux rope model of Kumar & Rust (1996), who found that a fraction of the magnetic free energy was converted to heat, and that the fraction depended on the flux rope parameters. Their model was a self-similar Lundquist solution, and as pointed out by Akmal et al. (2001) and Lee et al. (2009), self-similarity is not a good approximation so early in the CME eruption. In the MHD model of Lynch et al. (2004), excess magnetic free energy was dissipated until the CME approached a Lundquist flux rope at a height of 15 R_{sun}. Inspection of the EUVI-A and COR 1A images shows that the CME does not expand in a self-similar way, but the rough proportionality of the heating rate to the gain in kinetic and gravitational energy is the most plausible dependence for magnetic heating that we know of.

The wave heating models that matched the initial and final conditions had final temperatures near 16,000 K and required total heating of $(3.5–6.5) \times 10^{13}$ erg g^{-1}, or about 1500 times the coronal hole heating rate of Allen et al. (1998). However, these models cooled very rapidly to the 5000 K temperature floor of the models and reheated to temperatures where H could be excited only in the last 12 minutes before reaching the UVCS slit. Since the EUVI-A images show a gradual cooling, these models are not plausible. Models with the heating proportional to density reached temperatures near 18,500 K. They required 2.5 times more heat, but they also cooled to 5000 K and reheated during the latter half of the expansion, so we consider them to be implausible as well. Models with heating proportional to density squared did not produce an acceptable match. Finally, models with heating proportional to the increase in kinetic plus gravitational energy required $(4.4–7.2) \times 10^{14}$ erg g^{-1}, or about equal to the gravitational energy and 3 times the kinetic energy. These models cool rapidly at first due to radiative losses, then more slowly, with final temperatures around 20,000 K. These models match the general behavior of the EUVI-A images at the heights where the emission is bright enough to detect, and we consider them to be viable descriptions of the heating.

Overall, then, we find that heating above the height of the EIS slit required to match the UVCS observations is comparable to the heating needed to raise the gas to the temperatures observed by EIS and EUVI-A and to maintain it at those temperatures for a very minimal 10 minute timescale.

5. CONCLUSIONS

In the present work, we have analyzed coordinated observations of the early phases of a CME obtained with instruments on board of the *Hinode*, *SOHO*, and *STEREO-A* spacecrafts. We have measured the dynamics and three-dimensional trajectory of the CME plasma, determining the acceleration of the ejecta below 22 solar radii. We have also determined the density, mass, filling factor and thermal structure of the CME core, and have found that the CME core is made of two different plasma components moving coherently; EIS spectra have shown that these two components have different temperature, filling factor and density. UVCS observations have allowed us to monitor the physical properties of the ejected plasma at 1.9 solar radii. XRT images have shown that plasma at temperature between 5 and 10 MK are enveloping from below the bulk of the CME ejecta, although the temperature and the emission measure of this plasma are very uncertain due to contamination issues in the Al-poly filter and to the uncertainty in the relative EIS-XRT calibration.

The diagnostic results have allowed us to discuss the energy budget of the CME ejecta, and to evaluate the heating required to reach the measured plasma temperatures and to maintain them until at least 1.9 solar radii. The total heating is several times larger than the kinetic energy, so it is an important term in the energy budget. These requirements have been compared with predictions from theoretical models of CME heating and acceleration, and we found that our results allow us to rule out a few theoretical models proposed in the literature. Wave heating, thermal conduction, and heating by the internal shocks proposed by Filippov & Koutchmy (2002) cannot supply the required heating. Magnetic heating, shocks generated by outflows from the reconnection region, and energetic particles from the reconnection region remain viable heating mechanisms, but specific model predictions are needed before these ideas can be tested.

The work of E.L. is supported by the NNH06CD24C, NNG04ED07P, NNH09AL49I and other NASA grants. J.R.'s work was supported by NASA grant NNX09AB17G-R to the Smithsonian Astrophysical Observatory. The work of M.P.M. is supported by NASA grant NNX06AG95G to the Smithsonian Astrophysical Observatory. The authors acknowledge the help of Drs. R. Colaninno and G. Stenborg on the use of *STEREO* data, and Dr. A. van Ballegooijen for helpful discussions. *STEREO* is a project of NASA, *SOHO* is a joint ESA/NASA project. *Hinode* is a Japanese mission built and launched by JAXA/ISAS, collaborating with NAOJ as a domestic partner, NASA (USA), and PPARC (UK) as international partners. We warmly thank the anonymous referee for his/her valuable comments and suggestions that helped us greatly improve the paper.

APPENDIX

ELEMENTAL ABUNDANCES

The so-called "FIP effect" is the enhancement of the relative low-FIP/high-FIP element abundance in the corona over the photospheric value. Low-FIP elements are those with first ionization potential (FIP) <10 eV, while high-FIP elements have FIP>10 eV. Determining whether the FIP effect is present or not in the CME core is very important, because this effect can be used as a tracer of the origin of the ejected material.

Almost all the lines used for DEM determination are emitted by ions of low-FIP elements. Only O and He are a high-FIP elements, but their lines are the coldest in the data set listed in Table 6. This means that the relative abundances between low-FIP and high-FIP elements can only be measured for the coldest peak in the DEM, and even in that case with only one low-FIP element: Mg, which also receives a small contribution ($\simeq 5\%$–25%) from the peak at $\log T = 5.7$. We cannot determine the relative low-FIP/high-FIP for the other two peaks. The most accurate relative abundance ratio is Mg/O, as Mg V lines are formed at temperatures closer to O IV,V than to He II.

The results are variable with time, in the sense that for the first and the last of the spectra where the CME is visible, the FIP effect seems to be decreased by a factor 1.7 from the standard coronal value adopted for the DEM calculation. A decreased value of the FIP effect in prominences is in line with Skylab measurements obtained by Spicer et al. (1998). In the second and third data sets, on the contrary, the adopted coronal abundances are confirmed. This variability of the Mg/O relative abundance might indicate that plasma at different locations in the CME core either originates from different regions, or is fractionated during CME acceleration. However, given the uncertainties in the present measurement, no definitive conclusion can be reached.

REFERENCES

Akmal, A., Raymond, J. C., Vourlidas, A., Thompson, B., Ciaravella, A., Ko, Y.-K., Uzzo, M., & Wu, R. 2001, ApJ, 553, 922
Allen, L. A., Habbal, S. R., & Hu, R. 1998, J. Geophys. Res., 103, 6551
Andretta, V., & Jones, H. P. 1997, ApJ, 489, 375
Bemporad, A., Raymond, J. C., Poletto, G., & Romoli, M. 2007, ApJ, 655, 576
Brown, C. M., Feldman, U., Seely, J. F., Korendyke, C. M., & Hara, H. 2008, ApJ, 176, 511
Bryans, P., Landi, E., & Savin, D. W. 2009, ApJ, 691, 1540
Ciaravella, A., Raymond, J. C., Reale, F., Strachan, L., & Peres, G. 2001, ApJ, 557, 351
Culhane, J. L., et al. 2007, Sol. Phys., 243, 19
Dere, K. P., Landi, E., Mason, H. E., Monsignori Fossi, B. C., & Young, P. R. 1997, A&AS, 125, 149
Dere, K. P., Landi, E., Young, P. R., Del Zanna, G., Landini, M., & Mason, H. E. 2009, A&A, 498, 915
Feldman, U., Mandelbaum, P., Seely, J. L., Doschek, G. A., & Gursky, H. 1992, ApJS, 81, 387
Filippov, B., & Koutchmy, S. 2002, Sol. Phys., 208, 283
Forbes, T. G., et al. 2006, Space Sci. Rev., 123, 251
Gardner, L. D., Atkins, N., Fineschi, S., Smith, P. L., Kohl, J. L., Maccari, L., & Romoli, M. 2000, Proc. SPIE, 4139, 362
Gardner, L. D., et al. 1996, Proc. SPIE, 2831, 2
Gardner, L. D., et al. 2002, in The Radiometric Calibration of *SOHO*, ed. A. Pauluhn, M. C. E. Huber, & R. von Steiger (ESA SR-002; Noordwijk: ESA), 161
Golub, L., et al. 2007, Sol. Phys., 243, 63
Klimchuk, J. A. 2001, in Space Weather, ed. P. Song, H. Singer, & G. Siscoe (Geophysical Monograph 125; Washington, DC: AGU), 143
Kohl, J. L., Noci, G., Cranmer, S. R., & Raymond, J. C. 2006, A&AR, 13, 31
Kohl, J. L., et al. 1995, Sol. Phys., 162, 313
Kohl, J. L., et al. 1997, Sol. Phys., 175, 613
Kohl, J. L., et al. 1999, ApJ, 510, L59
Kumar, A., & Rust, D. M. 1996, J. Geophys. Res., 101, 15667
Landi, E., & Landini, M. 1997, A&A, 327, 1230
Lee, J.-Y., Raymond, J. C., Ko, Y.-K., & Kim, K. S. 2009, ApJ, 692, 1271
Lin, J. 2004, Sol. Phys., 219, 169

Lynch, B. T., Antiochos, S. K., MacNeice, P. J., Zurbuchen, T. H., & Fisk, L. A. 2004, ApJ, 617, 589
Rakowski, C. E., Laming, J. M., & Lepri, S. T. 2007, ApJ, 667, 602
Raymond, J. C., Cox, D. P., & Smith, B. W. 1976, ApJ, 204, 290
Shiota, D., Isobe, H., Chen, P. F., Yamamoto, T. T., Sakajiri, T., & Shibata, K. 2005, ApJ, 634, 663
Spicer, D. S., Feldman, U., Widing, K. G., & Rilee, M. 1998, ApJ, 494, 450
Watanabe, T., et al. 2009, ApJ, 692, 1294
Webb, D. F., & Jackson, B. V. 1981, Sol. Phys., 73, 341
Young, P. R., Watanabe, T., Hara, H., & Mariska, J. T. 2009, A&A, 495, 587
Zhang, M., & Low, C. B. 2005, ARA&A, 43, 103